



universität  
wien

# MASTERARBEIT

Titel der Masterarbeit

Laser Photodetachment in a Gas-Filled RF-Quadrupole

verfasst von

Johanna Pitters, BSc

angestrebter akademischer Grad

Master of Science (MSc)

Wien, 2015

Studienkennzahl lt. Studienblatt: A 033 876

Studienrichtung lt. Studienblatt: Physik

Betreuer: Univ.-Prof. Dipl.-Ing. Dr. Robin Golser



# Abstract

Accelerator Mass Spectrometry (AMS) is an ultra-sensitive technique for measuring the abundance of trace isotopes. For certain elements, isotopic ratios down to  $10^{-16}$  can be measured. The main challenge in AMS is the efficient suppression of isobars of the isotope of interest, i.e. nuclides of different elements with almost the same mass, that cannot be separated by the mass spectrometers.

A new approach for element-selective filtering is to use laser photodetachment for neutralization of the unwanted isobar species on the low energy side of the AMS machine and thus broaden the spectrum of accessible isotopes. In order to reach interaction times long enough for an efficient depletion, the ions are slowed down in a buffer gas filled RFQ ion guide. Inside the so-called cooler, the ion beam is overlapped with a high power, continuous wave laser beam. If the laser wavelength is chosen properly, the unwanted element is neutralized, while the ions of interest can be re-accelerated and injected into the AMS machine.

Such a cooler system for negative ions is being developed at the ILIAS laboratory, the Ion-Laser InterAction Setup. This Master's thesis describes the modifications made to the cooler system based on SIMION simulations, the commissioning of the ion beam cooler as well as first tests concerning the suppression of an ion beam by laser photodetachment.

By the end of the Master's project atomic and molecular negative ions had been cooled successfully. In photodetachment experiments with a copper beam a suppression of almost 5 orders of magnitude and an overall transmission of the cooler system of up to 44% could be demonstrated. Since the test bench is limited in space and identification methods after the cooler, the setup will soon be moved and connected to the AMS facility where the limitations of the method can be further explored. Once installed as an extension to VERA (Vienna Environmental Research Accelerator), laser photodetachment in the ion beam cooler is going to be used as an isobar filter in AMS measurements.



# Zusammenfassung

Beschleuniger-Massenspektrometrie (AMS) ist eine sehr empfindliche Methode zum Nachweis von Spurenisotopen. Für bestimmte Elemente können Isotopenverhältnisse bis zu  $10^{-16}$  bestimmt werden. Die große Herausforderung in der Beschleuniger-Massenspektrometrie besteht in der effizienten Unterdrückung der Isobare des gesuchten Isotops, also Nuklide eines anderen Elements mit fast derselben Masse, die von den Massenspektrometern nicht getrennt werden können.

Ein neuer Ansatz zur elementselektiven Trennung ist die Verwendung von Laserphotodetachment zur gezielten Neutralisierung der ungewollten Isobare auf der Niederenergieseite der AMS Anlage. Dadurch ließe sich das Spektrum der mit AMS zugänglichen Isotope deutlich erweitern. Um entsprechend lange Wechselwirkungszeiten für eine effiziente Unterdrückung zu ermöglichen werden die Ionen in einem mit Puffergas gefüllten RFQ ‘ion guide’ gebremst. In diesem sogenannten Ionenkühler wird der Ionenstrahl mit einem kontinuierlichen Hochleistungslaser überlagert. Bei geeigneter Wahl der Wellenlänge des Lasers werden die ungewollten Elemente neutralisiert, während das gesuchte Isotop wieder herausbeschleunigt und in die AMS Anlage eingeschossen werden kann.

Solch ein Ionenkühler für negative Ionen wird momentan im ILIAS Labor, dem Ion-Laser InterAction Setup, entwickelt. Diese Masterarbeit beschreibt die auf SIMION Simulationen beruhenden Änderungen am System, die Inbetriebnahme des Kühlers sowie erste Test-Experimente zur Unterdrückung eines Ionenstrahls durch Laserphotodetachment.

Bis zum Ende dieses Masterprojekts wurden atomare und molekulare negative Ionen erfolgreich gekühlt. In Photodetachment-Experimenten mit einem Kupferstrahl konnte eine Unterdrückung von nahezu 5 Größenordnungen und eine Transmission durch das Kühlsystem von bis zu 44% demonstriert werden. Da der Versuchsaufbau räumlich limitiert ist und nur begrenzte Mittel zur Teilchenidentifikation nach dem Kühler zur Verfügung stehen, wird der Aufbau bald an die AMS Anlage angeschlossen werden, wo die Grenzen der Methode weiter ausgelotet werden können. Sobald der Kühler in die Erweiterung von VERA (Vienna Environmental Research Accelerator) integriert ist, wird Laserphotodetachment im Ionenkühler als Isobarenfilter in AMS Messungen verwendet werden.



# Contents

<b>1. Introduction</b>	<b>1</b>
1.1. VERA - Vienna Environmental Research Accelerator . . . . .	1
1.2. Isobar Suppression in AMS . . . . .	3
1.2.1. Conventional Methods . . . . .	3
1.2.2. New Approaches to Element-Sensitive Isobar Suppression . . . . .	4
1.3. Laser Photodetachment of Negative Ions . . . . .	5
1.4. Isobaric Systems of Interest . . . . .	7
1.5. ILIAS - Ion Laser InterAction Setup . . . . .	9
<b>2. Linear Paul Trap</b>	<b>13</b>
2.1. Theoretical Description of the Linear Paul Trap . . . . .	13
2.1.1. Stability Criterion . . . . .	14
2.1.2. Motional Spectrum . . . . .	16
2.1.3. Optimum Trapping Conditions . . . . .	18
<b>3. Buffer Gas Cooling of Negative Ions</b>	<b>21</b>
3.1. Macroscopic Approach . . . . .	22
3.2. Microscopic Approach . . . . .	23
3.3. Simulation of Buffer Gas in SIMION 8.1 . . . . .	24
<b>4. ILIAS Ion Beam Cooler</b>	<b>29</b>
4.1. General Setup . . . . .	29
4.1.1. Injection . . . . .	29
4.1.2. Transport Through Cooler . . . . .	30
4.1.3. Extraction . . . . .	31
4.2. Electronics Setup . . . . .	32
4.2.1. Radio Frequency Setup . . . . .	32
4.2.2. Electronics Setup of the Guiding Electrodes . . . . .	33
4.3. Vacuum . . . . .	33
4.4. Guiding Electrodes . . . . .	34
4.4.1. Original Design . . . . .	35
4.4.2. Modification . . . . .	36
4.5. Injection and Extraction . . . . .	37
4.5.1. Original Design . . . . .	37
4.5.2. Modifications . . . . .	38
4.5.3. Simulation of Deceleration and Re-acceleration . . . . .	41
4.6. Transmission . . . . .	43
4.7. Tuning of the Cooler . . . . .	45
<b>5. Measurements and Results</b>	<b>47</b>
5.1. Original Design . . . . .	47

## Contents

---

5.2. Modification I . . . . .	50
5.3. Modification II . . . . .	51
5.4. Modification III . . . . .	55
<b>6. Summary and Outlook</b>	<b>59</b>
<b>A. SIMION Simulation of Buffer Gas Cooling</b>	<b>61</b>
A.1. Geometry . . . . .	61
A.2. Viscous Damping Model . . . . .	62
A.3. Hard-Sphere Model . . . . .	63
<b>Bibliography</b>	<b>69</b>
<b>Curriculum Vitae</b>	<b>73</b>

# 1. Introduction

Accelerator Mass Spectrometry (AMS) is the most sensitive method to measure trace amounts of long-lived radionuclides. Isotopic abundances down to  $10^{-12}$  -  $10^{-16}$  can be measured with high precision. The following exemplary list gives an insight to the broad range of applications of AMS, relevant to various fields of research.

- $^{14}\text{C}$  - dating of archaeological findings, environmental tracing
- $^{10}\text{Be}$ ,  $^{26}\text{Al}$ ,  $^{36}\text{Cl}$  - geological dating, e.g. exposure dating of rocks
- $^{60}\text{Fe}$  - detection of supernova traces
- $^{129}\text{I}$ ,  $^{236}\text{U}$  - environmental tracers of anthropogenic origins, e.g. tracing of ocean currents

A more comprehensive list of AMS-isotopes and their applications can be found in [1]. Classical decay counting is not convenient for measuring long-lived radioisotopes, because it requires either extremely large sample sizes or long counting times. For an AMS measurement  $\mu\text{g}$  to  $\text{mg}$  of target material are sufficient in order to reach satisfactory counting statistics within a reasonable measuring time of typically a few hours.

The advantage of AMS, as compared to conventional mass spectrometric methods (e.g. inductively coupled plasma MS, thermal ionization MS, secondary ion MS), is the effective suppression of atomic and molecular isobaric background and high efficiency at the same time. The requirement to the mass filter itself, consisting of an electrostatic and a magnetic deflector, is to separate the ion of interest from neighboring masses that are many orders of magnitude more intense. Atomic and molecular isobars are suppressed in a chain of consecutive filters (see section 1.2), enabling the measurement of rare isotopes. This thesis describes the development of a new, element-selective technique for isobar suppression. This new filter will extend the range of radionuclides accessible to AMS by enabling the measurement of isotopes that, for the methods available up to now, suffer from too strong isobaric background.

## 1.1. VERA - Vienna Environmental Research Accelerator

The Vienna Environmental Research Accelerator (VERA) is a state-of-the-art, middle-sized AMS facility, based on a 3 MV tandem accelerator. A schematic drawing of the VERA facility is shown in figure 1.1. There are two MC-SNICS (multi cathode source of negative ions by cesium sputtering) sources that can hold a target wheel with up to 40 samples. In the source the sample is sputtered with cesium and a negative ion beam of typically  $\mu\text{A}$  is extracted and pre-accelerated to about 70 keV. It is filtered by mass over charge ratio  $m/q$  in the low energy spectrometer, consisting of an electrostatic analyzer and the injection magnet. A voltage can be applied to the chamber of the magnet, which allows fast switching between the masses to be injected into the accelerator. The accelerator's terminal can be set to up to 3 MV. Inside the terminal, there is a stripper where the beam undergoes charge changing processes. After the stripper the beam has a

certain distribution of charge states and energies. The beam is filtered in the high energy spectrometer, selecting one charge state and eliminating the fragments from molecules, which break up in the stripper. The atomic, positively charged beam is further analyzed and detected.

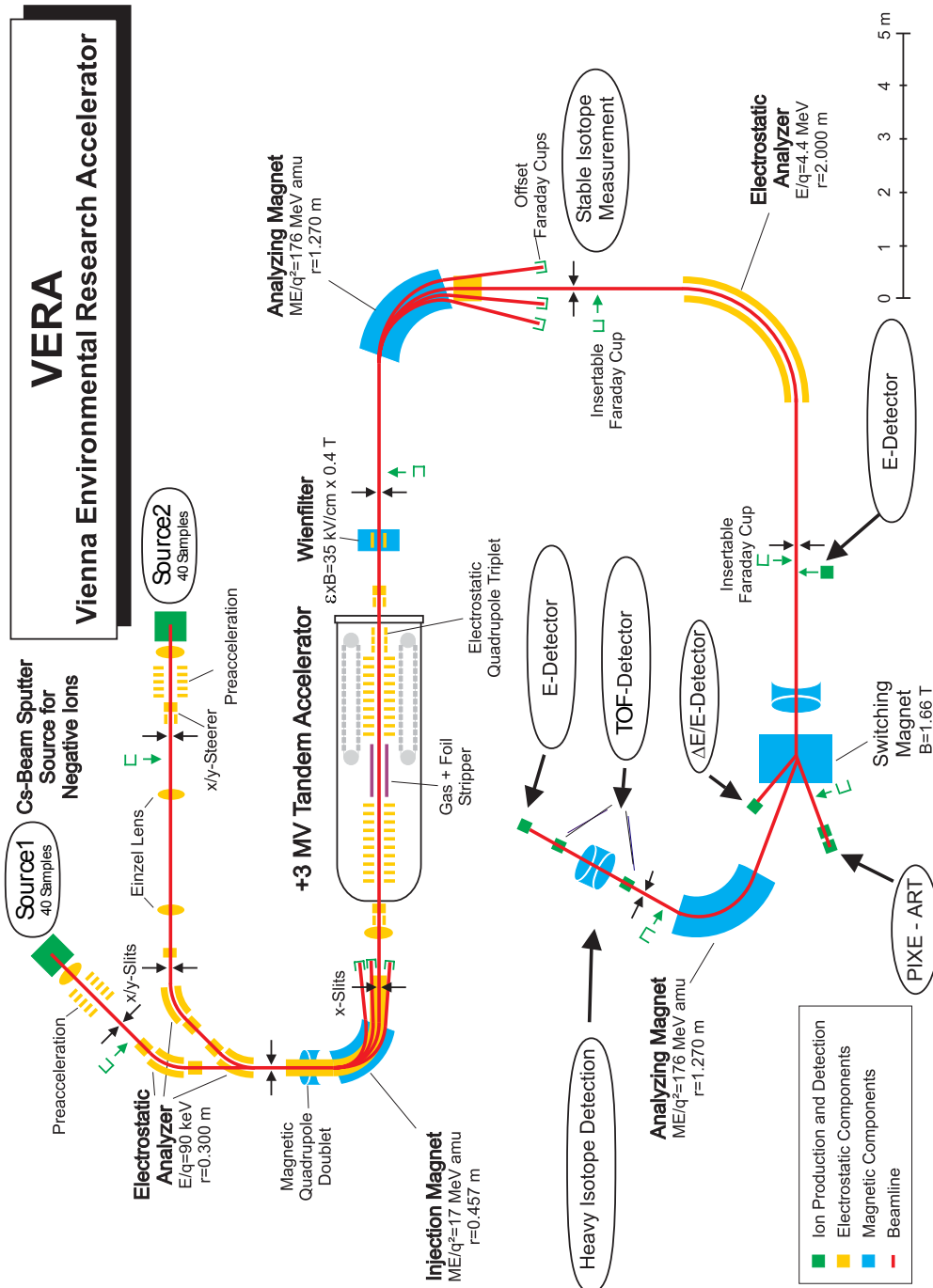


Figure 1.1.: Schematic drawing of the VERA facility.

## 1.2. Isobar Suppression in AMS

### 1.2.1. Conventional Methods

The first stage of isobar suppression happens in the ion source. Some elements, including all noble gases, have negative electron affinities and therefore do not form negative ions effectively. For example  $^{14}\text{N}$ ,  $^{26}\text{Mg}$  and  $^{129}\text{Xe}$ , the stable isobars of  $^{14}\text{C}$ ,  $^{26}\text{Al}$  and  $^{129}\text{I}$ , respectively, are suppressed in the source due to their lack of ability to form stable, negative ions. It has to be considered, that atomic and molecular ions have different electron affinities. There are cases where the atomic isobar forms negative ions, resulting in a strong background for the measurement. This background can be reduced by orders of magnitude by choosing an appropriate molecular ion, whose electron affinity is lower for the interfering isobar than for the isotope of interest. An example is  $^{182}\text{Hf}$  which suffers from stable background of  $^{182}\text{W}$ . When choosing  $\text{HfF}_5^-$  at the low energy side, the unwanted  $\text{WF}_5^-$  can be suppressed by a factor of  $3.6 \cdot 10^4$  in the source when sputtering  $\text{HfF}_4$  [2].

Background from molecular isobars can be eliminated by charge exchange processes and collisional break-up in the stripper inside the accelerator terminal. The stripper can be either a gas stripper or a foil stripper. A helium or argon gas stripper is used for most applications at the VERA facility. Molecules of higher positive charge are not stable, since chemical bonds are caused by the outermost electrons, which are stripped off in the charge changing process. In  $^{14}\text{C}$  dating, for example, the molecules  $^{12}\text{CH}_2$  and  $^{13}\text{CH}$  have the same mass number as the rare isotope  $^{14}\text{C}$ . The setting of the high energy mass spectrometer selects the charge state  $^{14}\text{C}^{3+}$ . The mass spectrometer filters out the fragments  $^{12}\text{C}$ ,  $^{13}\text{C}$  and H along with ions in charge states other than  $3+$ .

The stripping process can also be used for a separation of atomic isobars, given that the atomic number  $Z$  of the rare isotope is larger than that of the unwanted isobar. By fully stripping the radioisotope of interest, the isobar is eliminated since it cannot reach such a high charge state. The acceleration voltage limits the highest charge state available. Therefore this method is reserved for the largest AMS facilities exclusively and always suffers from low yields for the fully stripped charge state. It was successfully applied for example at the HRIBF (Holifield Radioactive Ion Beam Facility) in Oak Ridge for Cl measurements with a 25 MV tandem accelerator. [3]

After separation in the high energy spectrometer, isotopes and their isobars of the same charge have the same mass and energy and therefore the same velocity. They differ solely by their atomic number  $Z$  and can be distinguished by their different energy loss in matter. In general, one can use a passive degrader to induce a different energy loss of the ion species in the material. After the degrader they can easily be separated with a bending magnet or an electrostatic analyzer. Since the degrader acts as a stripper too, the technique suffers from low detection efficiency due to the splitting up into the charge states. If the atomic number of the unwanted isobar is higher than that of the rare isotope, an absorber can be put directly in front of the detector, in a such way, that the unwanted isobar is already stopped inside the absorber. At the VERA facility this is implemented by means of a SiN-foil stack before an ionization chamber for suppressing  $^{10}\text{B}$  against  $^{10}\text{Be}$  [4]. Isotopes that have higher  $Z$  than their isobar, like  $^{36}\text{Cl}$  and  $^{36}\text{S}$ , can be identified

in the MAIC detector, a multi-anode ionization chamber. It has three anodes, two for measuring the different energy losses of the particle species to be separated, and one for measuring the residual energy of each particle [5]. However, the measurement suffers from high count rates and energy spread due to angular scattering.

All methods based on the different energy loss in matter are limited by the ratio  $\Delta Z/z$  as well as the kinetic energy, which is required to overcome energy loss straggling. Both,  $\Delta Z/z$  and the available kinetic energy, have to be sufficiently high in order to reach an acceptable isobar separation. This strongly limits the range of radioisotopes accessible to AMS, especially for small and middle-sized AMS facilities like VERA, and implicates the need for new element-selective techniques in order to extend the range of accessible radioisotopes.

### 1.2.2. New Approaches to Element-Sensitive Isobar Suppression

There are two new, upcoming approaches to element-sensitive isobar suppression under investigation, based on interaction of negative ions with either a reactive gas or with a laser. Both methods work with low-energy, negatively charged ions and shall be installed on the low energy side of an AMS machine.

Investigations concerning isobar suppression through ion-gas interactions as well as the development of a reaction cell system are carried out at the A.E. Lalonde AMS Laboratory at University of Ottawa, former IsoTrace Lab at University of Toronto. The commercial Isobar Separator for efficient isobar suppression by ion-gas reactions, based on a segmented RFQ (radio frequency quadrupole) ion guide, is being developed by Isobarex Corporation, Bolton, Ontario, Canada, in collaboration with the A.E. Lalonde AMS Lab. The underlying process is the resonant electron exchange between an anion and a gas. As reactive gases for example  $O_2$ ,  $N_2$  or  $NO_2$  are used. The cross section for an electron exchange process is related to the chemical properties of anion and gas, hence, it is element-sensitive (neglecting very small isotopic effects). For efficient separation of isobars, the anions have to be decelerated to energies as low as eV.

An older version of the Isobar Separator consisted of four RFQ-sections: the decelerator, where the ion energy is reduced to 20 eV, the cooler-section, where the ion energy is further reduced below 1 eV by collisional cooling, the reaction cell, filled with the reactive gas, and a mass selector [6]. Later the cooler-section was abandoned for a single cell, used for both, cooling and ion-gas reactions, enabling a suppression of S versus Cl by 6 orders of magnitude using  $NO_2$  as a reactive gas [7].

For the latest update of the Isobar Separator, the gas-filled section is implemented as a segmented RFQ. Acceleration gaps are used to compensate the cooling effect in order to maintain a constant ion energy in the range of 1-3 eV, which turns out to be crucial for certain applications as the separation of  $KF_3^-$  from  $CaF_3^-$ . [8]

The second approach towards element-selective isobar suppression is optical filtering. Laser photodetachment of negative atomic or molecular ions can be used to neutralize unwanted isobars, provided that the detachment energy of the radioisotope of interest is higher than the one of the unwanted isobar. Proof of principle was already demonstrated in 1989 by Berkovits et al [9]. They measured suppression ratios of one order of magnitude

for S/Cl with a laser of 532 nm wavelength (2.33 eV) [9] and two orders of magnitude for Ni/Co using a wavelength of 1064 nm (1.17 eV) [10]. For both measurements the laser was operated in a pulsed mode with a low duty cycle. In order to improve the detachment efficiency dramatically, the interaction time between ions and laser has to be extended. For this purpose, the ions can be decelerated in a gas-filled RFQ ion guide where the beam is cooled down to thermal energies by collisions with a He buffer gas. This approach has been demonstrated by Liu et al. at the Oak Ridge National Laboratory [11]. Such a cooler system for negative ion beams is being realized as an extension to the AMS facility VERA. The further development of the cooler system as well as first demonstration experiments on isobar suppression by laser photodetachment are the subject of this work.

### 1.3. Laser Photodetachment of Negative Ions

The electron affinity EA is defined as the energy difference between the ground states of an atomic negative ion  $A^-$  or a molecular negative ion  $R^-$  and its corresponding neutral A or R, respectively. In case of a molecule, 'ground state' refers to the vibrational and rotational ground state  $|v = 0, J = 0\rangle$ .

$$EA(A) = \Delta E(A \leftarrow A^-) \quad (1.1)$$

$$EA(R) = \Delta E(|R, v' = 0, J' = 0\rangle \leftarrow |R^-, v'' = 0, J'' = 0\rangle) \quad (1.2)$$

For molecules, this 'adiabatic' electron affinity is often not directly accessible to experiments, but the vertical detachment energy (VDE) and the vertical attachment energy (VAE) can provide upper and lower limits for the electron affinity. They refer to the energy difference between the ground state of the anion or neutral and an excited state of the neutral or anion, respectively (see figure 1.2).

Photodetachment is the process of removing an electron from a negative ion by means of laser radiation:



where  $h$  represents Planck's constant and  $\nu$  the frequency of the incoming photon. It is a threshold process and can occur as soon as the photon has an energy equal or larger than the electron affinity of the atom, assuming the anion is in its ground state. If it is in an excited state, the threshold for photodetachment is shifted towards lower photon energies.

The energy dependence of the cross section is given by the electronic configurations of the negatively charged ion and the neutral atom or molecule. Around the threshold it is described by Wigner's law

$$\sigma(E) = 0 \quad \text{for } E < E_{TH} \quad (1.4)$$

$$\sigma(E) \propto (E - E_{TH})^{L+1/2} \quad \text{for } E > E_{TH} \quad (1.5)$$

where  $L$  is the angular momentum of the photoelectron and  $E_{TH}$  is the energy threshold of the reaction [13]. For  $L = 0, 1, 2, \dots$  the photoelectron is called  $s, p, d, \dots$ -wave electron, respectively. Figure 1.3 shows the cross section for photodetachment as described by the Wigner-law near the threshold.

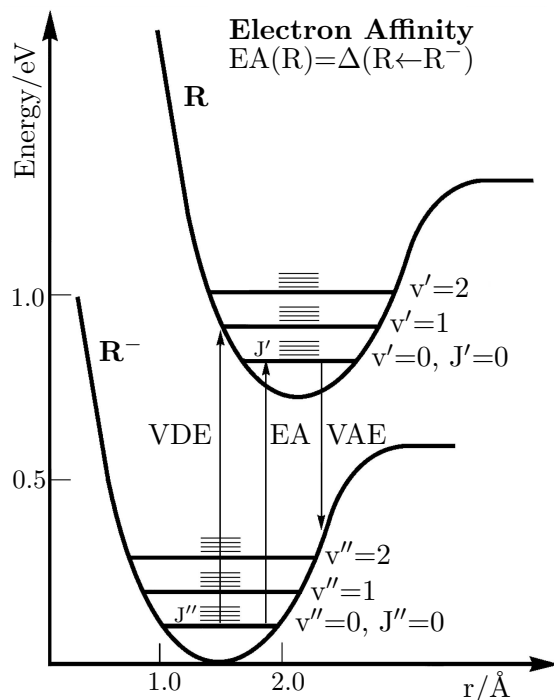


Figure 1.2.: Qualitative diagram of potential energy surfaces for an anionic molecule  $R^-$  and a neutral molecule  $R$ . Figure taken from [12].

The most common methods to determine electron affinities experimentally are threshold studies and photoelectron spectroscopy. Therefore a negative ion beam is overlapped with a laser beam either collinearly or in a crossed beams setup. The advantage of the crossed beams is that the Doppler shift does not have to be taken into account for a  $90^\circ$  geometry. For the threshold study the laser frequency is scanned. The number of neutralized particles as a function of photon energy gives a measure of the cross section for photodetachment. For photoelectron spectroscopy, the laser frequency is fixed. The photoelectrons are collected and their kinetic energy is measured.

As a demonstration experiment, a photodetachment study of  $C^-$  was realized in a crossed beams configuration at the ILIAS Laboratory [14]. An infrared 10 W fiber coupled diode laser with a nominal wavelength of 984 nm, corresponding to 1.26 eV, was used. By varying the temperature of the laser diode, the wavelength can be shifted by 16 nm, thus covering the threshold region for photodetachment of  $C^-$ . The electronic configurations of the negative atomic state and neutral atom are,

$$\begin{aligned}
 (2p^3) \ ^4S_{3/4} & \quad \text{for } C^- \\
 (2p^2) \ ^3P_0 & \quad \text{for } C
 \end{aligned}$$

resulting in  $\Delta L = 1$ . Since the photon has angular momentum  $l = 1$ , the photoelectron has  $L = 0$ , thereby being an s-wave electron. The measured values and the fit for s-wave detachment is given in figure 1.4. The electron affinity as deduced from the fit is 1.26257(9), deviating from the literature value given in table 1.1) by only 0.04%.

Electron affinities that have not yet been determined in photoelectric experiments can be computed by density functional theory [12]. The method gives predictions within an accuracy of typically 0.2 eV. It is therefore a convincing method for large molecules that

are not easily accessible to experiments.

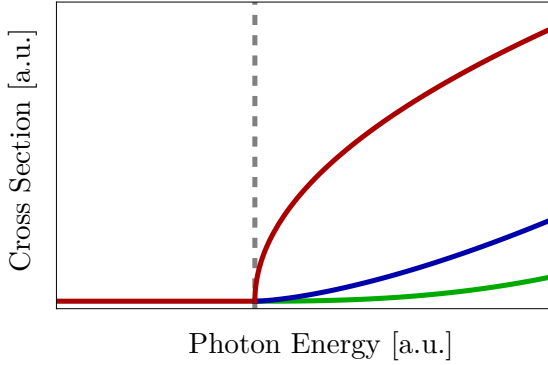


Figure 1.3.: Schematic of the cross section for s-wave (red), p-wave (blue) and d-wave (green) photodetachment around threshold (dashed line).

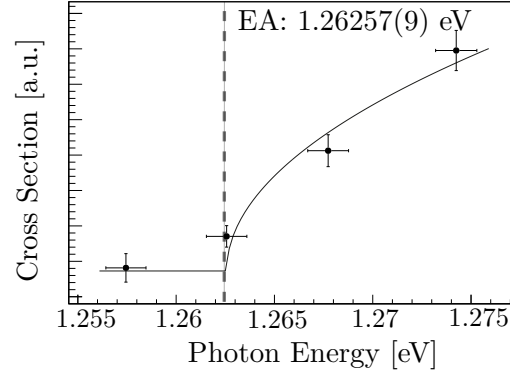


Figure 1.4.: Threshold study of  $C^-$  at ILIAS with an infrared diode laser. The electron affinity was deduced from a fit according to Wigner's law.

## 1.4. Isobaric Systems of Interest

In this section a short introduction to some selected isobaric systems that are of special interest in the context of laser-assisted AMS shall be given. Table 1.1 gives values for the corresponding electron affinities.

$^{26}\text{Al}$  is routinely measured at the VERA lab and many other AMS laboratories. Its stable isobar  $^{26}\text{Mg}$  does not form negative ions due to its negative electron affinity and is therefore suppressed in the source. However, the output of  $\text{AlO}^-$  is 10 to 20 times higher than that of the atomic negative ion  $\text{Al}^-$  [15]. If the molecular isobar  $\text{MgO}^-$  could be suppressed by laser photodetachment, the oxide could be used to form a negative beam on the low-energy side of the AMS machine. The efficiency of laser photodetachment of  $\text{MgO}^-$  and the overall transmission of  $\text{AlO}^-$  through the cooler system decide over success and failure.

$^{36}\text{Cl}$  is also a well-established AMS isotope. The separation from its isobar  $^{36}\text{S}$  is possible via their different energy loss in matter, using a segmented ionization chamber (see section 1.2.1). The use of laser photodetachment, will reduce the background count rate in the detector and thereby speed up measurements. Also, it states a perfect test case of an atomic isobaric system.

$^{60}\text{Fe}$  can so far only be measured at two of the largest AMS machines worldwide, namely the Maier-Leibnitz-Laboratory at TUM, Munich [16], and the Heavy Ion Accelerator Facility at ANU, Canberra [17]). High particle energies are required to efficiently separate  $^{60}\text{Fe}$  from its stable isobar  $^{60}\text{Ni}$  ( $\Delta Z/Z = 1/14$ ) on the high-energy side. Unfortunately Ni has a higher electron affinity than Fe (see table 1.1), so laser photodetachment cannot be applied to suppress the atomic isobar. The situation is reversed for the corresponding single hydrides:  $\text{FeH}$  has a higher electron affinity than  $\text{NiH}$  and is therefore suitable for optical filtering. It has been demonstrated that the use of these hydrides on the injection

side is not only possible, but also favorable because the background from  $\text{NiH}^-$  is reduced by a factor of 500 in the source, resulting in a detection limit of  $^{60}\text{Fe}/\text{Fe}$  of  $10^{-11}$  [18]. Optical filtering of the hydrides makes the measurement of  $^{60}\text{Fe}$  possible at facilities of smaller terminal voltage.

$^{135}\text{Cs}$  suffers from interference of stable  $^{135}\text{Ba}$ . They can not be separated with conventional methods for isobar suppression (see section 1.2.1). The low  $\Delta Z/Z$  hinders sufficient separation based on energy loss in matter. Optical filtering has the potential to enable an efficient suppression of the atomic negative isobar  $^{135}\text{Ba}^-$ .

$^{182}\text{Hf}$  is an extinct radionuclide with a half-life of 8.9 million years [19]. It could be used as indicator for a recent supernova, but the expected low ratio of  $^{182}\text{Hf}/^{180}\text{Hf}$  of  $10^{-12}$  [20] can so far not be measured. The electron affinity of Hf is close to zero, therefore it does not form atomic negative ions efficiently. However, the fluorides are suitable for production of negative ion beams.  $^{182}\text{HfF}_5^-$  has a high production yield, while the background due to  $^{182}\text{W}$  is strongly suppressed, resulting in a detection limit of  $10^{-12}$  for the  $^{182}\text{Hf}/^{180}\text{Hf}$  ratio [2]. Chen et al. [21] have calculated the vertical detachment energies of the pentafluorides using ab initio methods. They have published values of 8.8 eV for  $\text{HfF}_5$  and 3.9 eV for  $\text{WF}_5$ . Unfortunately these values have never been confirmed experimentally. Latest experiments at GUNILLA (Gothenburg University Negative Ion Laser Laboratory) have shown that the photodetachment cross section for  $\text{WF}_5^-$  is at least 100 times larger than for  $\text{HfF}_5^-$  at a wavelength of 266 nm (corresponding to 4.7 eV) [22].

Atom or Molecule	Electron Affinity [eV]	Reference
C	1.262119(20)	[12]
Cu	1.23579(4)	[12]
Al	0.43283(5)	[12]
Mg	<0	[13]
AlO	2.60(1)	[12]
MgO	1.622(10)	[23]
Cl	3.612724(3)	[12]
S	2.077103(3)	[12]
Fe	0.151(3)	[12]
Ni	1.15706(12)	[12]
FeH	0.934(11)	[12]
NiH	0.481(7)	[12]
Cs	0.47164(6)	[12]
Ba	0.14462(6)	[12]
Hf	$\sim 0$	[13]
W	0.187(4)	[12]
$\text{HfF}_5$	<i>8.8</i>	[21]
$\text{WF}_5$	<i>3.9</i>	[21]

Table 1.1.: Electron affinities for some atoms and molecules of interest. Values in italics are vertical detachment energies calculated with ab initio methods and have not yet been confirmed experimentally.

## 1.5. ILIAS - Ion Laser InterAction Setup

ILIAS, the Ion Laser InterAction Setup, is dedicated to photodetachment studies and the development of an ion beam cooler for negatively charged atomic and molecular ions. The ion beam cooler is going to be moved and connected to the VERA facility in the near future. Up to now, ILIAS is a setup located in a basement laboratory and is run completely independently from VERA. Figure 1.5 shows a schematic drawing of the ILIAS setup.

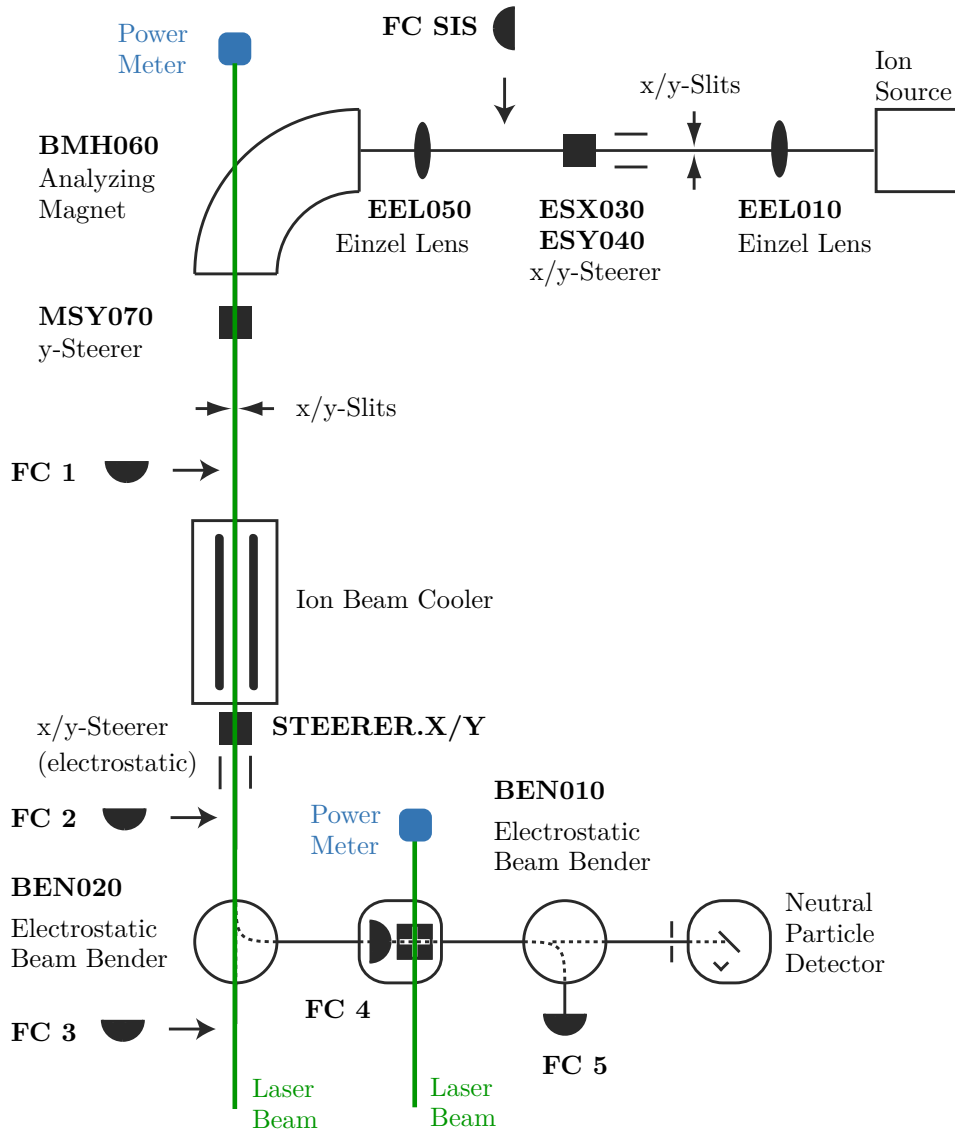


Figure 1.5.: Schematic drawing of the ILIAS setup.

### Injector

A single cathode cesium sputter ion source (SNICS II) is used to produce a negative ion current of typically  $\mu\text{A}$ . The kinetic energy of the ions of up to 30 keV is determined by the source potential, which is given as the sum of the source high voltage (SIS.HVS), and the cathode voltage (SIS.CAT). The source together with the  $90^\circ$  double focusing bending magnet (BMH060) form a negative ion spectrometer that provides mass-separated beams for injection into the ion beam cooler. With a radius of  $\rho=0.75$  m and a maximum field of 0.8 T, the magnet is capable of bending singly charged ions with masses up to 580 amu at 30 keV. It has two view ports: one provides direct sight into the source, through the other one the laser beam can exit the beamline. Between the source and the magnet two electrostatic einzel lenses (EEL010 and EEL050), slits and electrostatic steerers for both, x- and y-direction (ESX030 and ESY040), are available. After the magnet there is a magnetic y-steerer (MSY070) and a pair of insulated slits. The insertable Faraday cups and the slits are the only diagnostics elements before injection into the cooler.

### Ion Beam Cooler

The whole beamline section that holds the cooler is separated from the rest of the beamline by ceramic insulators and is surrounded by a HV safety cage. The section inside the cage can be put on cooler high voltage (RFQ.HV) of up to  $-30$  kV. All power supplies for cooler elements, namely the injection lenses (INJHI and INJLO), the extraction lenses (EXTHI and EXTLO) and the guiding electrodes (GELEC) are placed inside the cage, with their ground being on cooler potential. Also placed inside the cage is a module of the control system and the RF setup including the function generator and the power amplifier. All components inside the cage are provided with 220 V AC power via an isolation transformer that separates the lab ground from cooler ground. Data is transmitted via an optical fiber. A more detailed description of the ion beam cooler is given in chapter 4.

### Detection Setup

After the cooler section, the beam can be bent two more times by  $90^\circ$  electrostatic deflectors (BEN020 and BEN010). A neutral particle detector is needed to detect particles that were neutralized by the probe laser (see below). A detailed description of the detection setup and the neutral particle detector can be found in [14]. The positioning of the various Faraday cups (FC) is shown in figure 1.5.

The electrostatic x/y-deflector right after the cooler section was included only at a later stage. It was only used in the very last measurements described in this thesis. Its implementation was essential for the correction of any misalignment following the cooler and thereby for improving the transmission from FC 2 to FC 4 and FC 5.

### Laser Setup

Currently there are two continuous wave lasers available at the ILIAS Laboratory.

- 984 nm (infrared) fiber coupled diode laser, FC-W-915, CNI, 10 W
- 532 nm (green) diode-pumped solid-state laser, VERDI V18, Coherent, 18 W

For a maximum ion-laser overlap inside the cooler, the laser beam is tuned through the cooler apertures by maximizing the laser power measured in the power meter after the

analyzing magnet. The power meter is a thermal power sensor from ThorLabs, model S310C. For verification purposes a second ion-laser overlap with the so-called probe laser can be realized either in a crossed beams setup, as marked in figure 1.5, or collinearly along the line between the electrostatic benders and the neutral particle detector.

During this work only the green laser (532 nm) was overlapped in the main interaction region inside the cooler. So far the probe laser has not been used in any experiment with the ion beam cooler. A certain fraction of laser power is lost on the apertures, mirrors and windows. At maximum laser power output (18 W), up to 12 W could be transmitted through the cooler system into the power meter. Considering the losses on the exit window and the beam injection aperture, the laser power inside the ion beam cooler is expected to be about 20% higher than the transmitted power.



## 2. Linear Paul Trap

Earnshaw's theorem is a fundamental principle in electrostatics stating that it is impossible to create a stable potential minimum from static electric or magnetic fields [24]. As a result, charged particles can be confined neither by static electric fields, nor by static magnetic fields alone. Two basic principles are most commonly used for confining particles:

- **Penning traps** use a superposition of a static electric quadrupole field and a homogeneous magnetic field to confine charged particles in three dimensions. Penning traps are for example used for measuring masses, g-factors or hyperfine structure separations with high precision.
- **Paul traps** create a confining potential for charged particles using time-dependent electric fields. 2 or 3 dimensional traps can be realized with the appropriate electrode geometry. Here the case of the two dimensional Paul trap is discussed.

### 2.1. Theoretical Description of the Linear Paul Trap

For better understanding of the cooler and the requirements on the operating parameters, the theoretical description of a single, charged particle in a linear Paul trap is given in this section. In order to trap the particle one can assume a potential that creates a restoring force proportional to the particle's displacement  $\vec{r} = (x, y, z)$ .

$$\vec{F} \propto -k \cdot \vec{r} \quad (2.1)$$

If this force originates from an electric field  $\vec{E}$ , acting on a particle of charge  $Q$ , the problem can be reduced to finding an appropriate electric potential  $\Phi$ .

$$\vec{F} = Q \cdot \vec{E} = -Q \cdot \vec{\nabla} \Phi \quad (2.2)$$

In charge free space  $\Phi$  has to satisfy Laplace's equation.

$$\Delta \Phi = 0 \quad (2.3)$$

As an ansatz one can chose the potential

$$\Phi = \frac{\Phi_0}{r_0^2} (\alpha x^2 + \beta y^2 + \gamma z^2) \quad (2.4)$$

with  $\alpha$ ,  $\beta$  and  $\gamma$  being some constants,  $r_0$  a normalizing factor and  $\Phi_0$  an arbitrary function. Inserting this potential (equation 2.4) into Laplace's equation (equation 2.3) gives a restriction on the constants.

$$\alpha + \beta + \gamma = 0. \quad (2.5)$$

The case  $\alpha = \beta = 1$  and  $\gamma = -2$  describes the ideal 3-dimensional Paul trap. Here only the 2-dimensional trap is discussed, where  $\alpha = -\beta = 1$  and  $\gamma = 0$ . The resulting potential

$$\Phi = \frac{\Phi_0}{r_0^2}(x^2 - y^2) \quad (2.6)$$

creates a force that is proportional to the displacement, as assumed in the beginning. However, this force is restoring in one direction only, while it is repulsive in the perpendicular direction. An overall confined particle motion can be achieved by inserting a time-dependent potential of the form

$$\Phi_0(t) = U + V \cos(\omega t) \quad (2.7)$$

into equation (2.2), giving the force  $\vec{F}$  on the particle.

$$\vec{F} = -Q \cdot \vec{\nabla} \Phi = -\frac{2Q}{r_0^2} (U + V \cos(\omega t)) \begin{pmatrix} x \\ -y \end{pmatrix} \quad (2.8)$$

The equation of motion of a particle moving under the influence of such a force can be calculated, as demonstrated here for the coordinate  $u$  which can be either  $x$  or  $y$ .

$$F = m \cdot a = m \cdot \ddot{u}(t) = -\frac{2Q}{r_0^2} (U + V \cos(\omega t)) u(t) \quad (2.9)$$

The substitution  $\omega t \rightarrow 2\tau$  leads

$$\ddot{u}(\tau) + \left( \frac{8QU}{mr_0^2\omega^2} + \frac{8QV}{mr_0^2\omega^2} \cos(2\tau) \right) u(\tau) = 0 \quad (2.10)$$

which can be rewritten as

$$\ddot{u}(\tau) + (a - 2q \cos(2\tau)) u(\tau) = 0 \quad (2.11)$$

using parameters  $a$  and  $q$ .

$$a_x = -a_y = \frac{8QU}{mr_0^2\omega^2} \quad q_x = -q_y = -\frac{4QV}{mr_0^2\omega^2} \quad (2.12)$$

Equation (2.11) is the wave equation in elliptical coordinates (after separation) and is usually referred to as *Mathieu equation*. Its solutions are well-known, describing the motion of an elliptical membrane. In practice,  $r_0$  corresponds to the distance from the axis to the quadrupole electrodes. The parameters  $a$  and  $q$  (equation 2.12) are called *Mathieu parameters* and show the correlation between the particle's mass and the operating parameters of the quadrupole (RF voltage, RF frequency and DC voltage).

### 2.1.1. Stability Criterion

In the following some general properties of solutions of the Mathieu equation are given, in order to obtain a stability criterion for the particles in a 2D Paul trap. A complete description of the Mathieu equation and its solutions can be found in [25] and [26].

## 2.1. Theoretical Description of the Linear Paul Trap

All solutions that satisfy  $f(t + \pi) = \pm f(t)$  are so-called “basically periodic solutions” referred to as *Mathieu functions*. They fall in 4 classes.

$ce_n(\tau, q) \rightarrow \text{odd, period } \pi$	with $n = 2k, k \in \mathbb{N}$
$ce_n(\tau, q) \rightarrow \text{odd, period } 2\pi$	with $n = 2k + 1, k \in \mathbb{N}$
$se_n(\tau, q) \rightarrow \text{even, period } \pi$	with $n = 2k, k \in \mathbb{N}_+$
$se_n(\tau, q) \rightarrow \text{even, period } 2\pi$	with $n = 2k + 1, k \in \mathbb{N}$

All  $ce_n(\tau, q)$  and  $se_n(\tau, q)$  are Fourier polynomials of order  $n$  including only cosine or sine functions, respectively. These basically periodic solutions exist only for certain values of the Mathieu parameters  $a$  and  $q$ .

For  $q \in \mathbb{R}$  the following statements are true for the Mathieu parameter  $a$ .

- All values of  $a$  that give rise to basically periodic solutions for a certain value of  $q$  are called *characteristic numbers*.
- All characteristic numbers are real;  $a \in \mathbb{R}$ .
- All characteristic numbers are finite if  $q$  is finite;  $a < \infty$ , if  $q < \infty$ .
- For  $q = 0$ , all basically periodic solutions reduce to multiples of  $\cos(n\tau)$  and  $\sin(n\tau)$  and  $a(q) = n^2$  with  $n \in \mathbb{N}$ .
- The characteristic numbers are continuous functions  $a(q)$ , called *Mathieu characteristics*. They are denoted by

$$\begin{aligned} a_n(ce_n(\tau, q)) & \quad \text{with } n \in \mathbb{N} \\ b_n(se_n(\tau, q)) & \quad \text{with } n \in \mathbb{N}_+ \end{aligned}$$

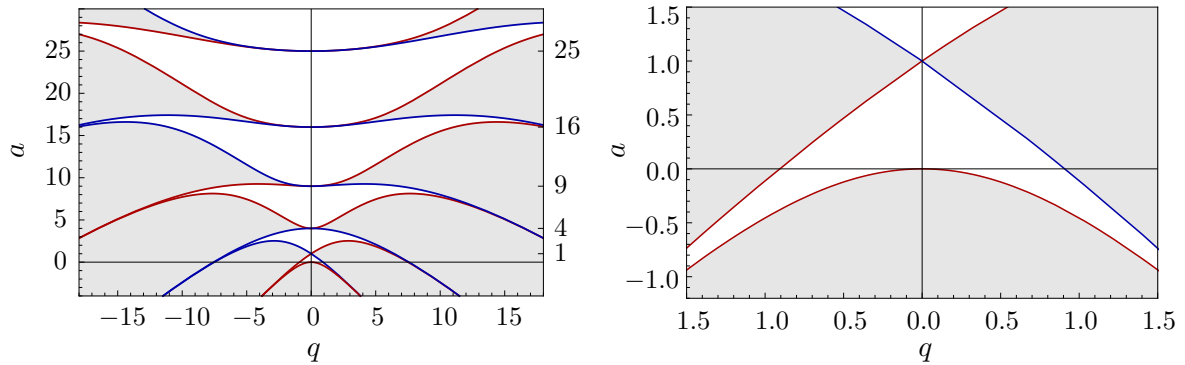


Figure 2.1.: Stability domains of the Mathieu equation with Mathieu characteristics  $a_n$  (red) and  $b_n$  (blue), white: stable regions, gray: unstable regions, right: enlarged.

Stable solutions to the Mathieu equation exist only for

$$\begin{aligned} q > 0, & \quad a_n < a < b_{n+1} \\ q = 0, & \quad a > 0 \\ q < 0, & \quad a_{2n} < a < a_{2n+1} \text{ and} \\ & \quad b_{2n+1} < a < b_{2n} \end{aligned}$$

with the Mathieu characteristics marking the edge of the stable regions. In figure 2.1 the stability domains are shown. For stable ion trajectories, both,  $x$ - and  $y$ -stability have to be considered. Since  $a \rightarrow -a$  and  $q \rightarrow -q$  for  $x \rightarrow y$ , the regions of overall stability are the overlap of the stable regions of the stability diagram and its mirroring along the  $q$ -axis. The largest region of overall stability is bordered by the Mathieu characteristics  $-a_0(q)$  and  $b_1(q)$  for positive values of  $a$  and  $q$  (figure 2.2). Since the stable domains are symmetric along both axes, one does not need to worry about the sign of  $a$  and  $q$ .

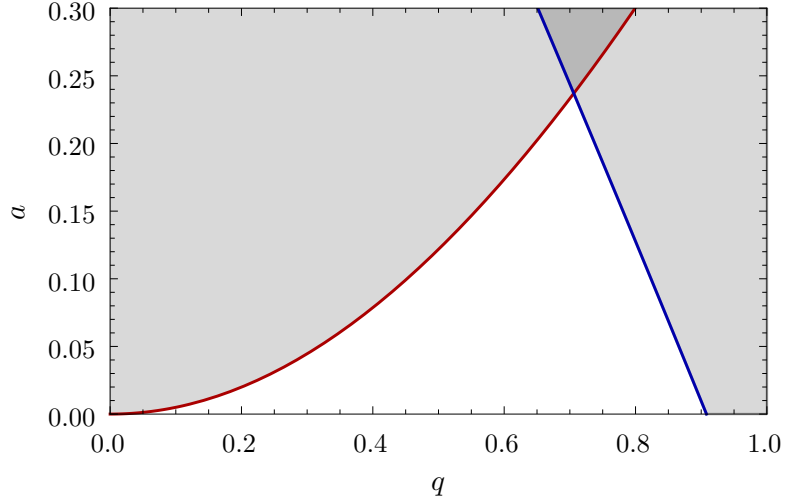


Figure 2.2.: Stability domain for  $x$ - and  $y$ -movement; Mathieu characteristics  $-a_0(q)$  (red) and  $b_1(q)$  (blue), white: stable region, light gray: stable only for  $x$ -movement (left) or  $y$ -movement (right), dark gray: unstable region.

In the case of an ion guide (in contrast to the quadrupole mass filter) no DC voltage is applied, so  $a = 0$ . For all  $|q| < 0.908$  the particle trajectories are stable in both,  $x$ - and  $y$ -direction. Having equation 2.12 in mind this means that for any fixed RF frequency and RF amplitude, the ion guide acts as a high-pass mass filter, selecting all

$$m > \left| \frac{0.908 \cdot r_0^2 \omega^2}{4QV} \right|. \quad (2.13)$$

### 2.1.2. Motional Spectrum

All stable solutions of equation 2.11 can be expressed as Fourier series. Let  $u$  be either  $x$  or  $y$ .

$$u(\tau) = A \sum_{n=-\infty}^{+\infty} c_{2n} \cos[(\beta + 2n)\tau] + B \sum_{n=-\infty}^{+\infty} c_{2n} \sin[(\beta + 2n)\tau] \quad (2.14)$$

## 2.1. Theoretical Description of the Linear Paul Trap

---

$A$  and  $B$  are constants that depend on the initial condition  $u(0)$ .  $\beta$  is the stability parameter and  $c_{2n}$  are the amplitudes of the Fourier components. Both can be obtained by recursion formulas. Here only the *adiabatic approximation*, that implies that the field variation is negligible over the amplitude of the particle oscillation, is being considered. This approximation is valid for  $a, q \ll 1$ . The stability parameter can be approximated by

$$\beta^2 \approx a + \frac{q^2}{2} \quad (2.15)$$

and the coefficients  $c_{2n} \propto q$  become rapidly smaller with increasing  $n$ , so higher order terms can be neglected. The equation of motion reduces to

$$u(t) = C \left( 1 - \frac{q}{2} \cos(\omega t) \right) \cos \left( \frac{\beta\omega}{2} t \right) \quad (2.16)$$

with  $C$  depending on the initial conditions and  $\omega$  being the driving frequency of the RF field. Equation 2.16 describes the particle motion as a superposition of two oscillations. The *macromotion* of frequency  $\Omega = \frac{\beta\omega}{2}$  is rather slow, since  $\beta \ll 1$ . Its amplitude is modulated at the frequency  $\omega$  of the driving field. This modulation is called *micromotion* due to its small amplitude ( $q \ll 1$ ). [24]

Figure 2.3 shows particle trajectories simulated in SIMION for different values of the Mathieu parameter  $q$ , with  $a = 0$ . For small values of  $q$ , the motion is well described by the large-amplitude macromotion, modulated by the micromotion, while for larger values of  $q$ , the weight of the amplitudes shifts and the amplitude of the high-frequency oscillation is modulated with lower frequency.

In the simulation, particle trajectories with a Mathieu parameter of up to  $q = 0.96$  are stable. According to Denison [27] the region of stability is shifted towards higher values of the Mathieu parameters if the field configuration deviates from the pure quadrupole field. This applies also to the case of the ILIAS cooler which is equipped with circular rather than hyperbolic RF rods. Also the guiding electrodes change the field configuration.

For an “RF only” potential where  $U = 0$  and thus  $a = 0$ , the macromotion can be described as an oscillation of frequency

$$\Omega_{a=0} = \frac{q}{\sqrt{8}} \Omega \quad (2.17)$$

in a radial pseudo-potential well

$$\Phi_P(r) = \frac{qV}{4r_0^2} r^2 \quad (2.18)$$

of depth

$$D = \frac{qV}{4}. \quad (2.19)$$

The adiabatic approximation is used in [28, 29, 30] and discussed in detail in [24]. According to Liu et al. [29] the pseudo-potential is a good approximation for all  $q \lesssim 0.4$ .

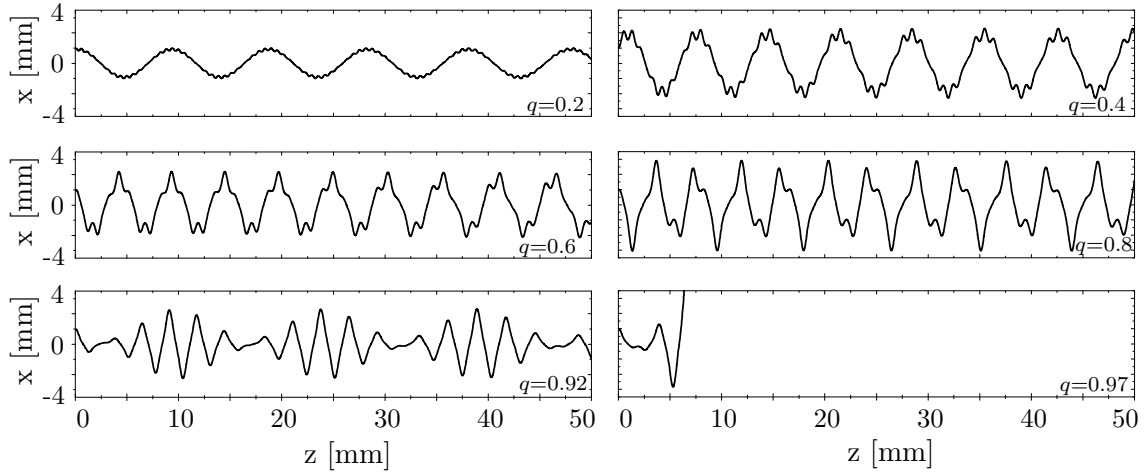


Figure 2.3.: Trajectories in the ILIAS cooler without buffer gas for different values of the Mathieu parameter  $q$  ( $m=36$ , RF amplitude=200 V). The smallest distance between opposite RF rods is 8.74 mm. For small values of  $q$ , the motion is well described by the large-amplitude macromotion, modulated by the micromotion, while for larger values of  $q$ , the weight of the amplitudes shifts and the amplitude of the high-frequency oscillation is modulated with lower frequency. For  $q > 0.96$  the motion gets unstable.

### 2.1.3. Optimum Trapping Conditions

The maximum number of particles to be confined in a trap of a given size is limited by space charge. The space charge potential cannot exceed the depth of the pseudo potential well. Thus, according to equation 2.19, large values of  $q$  are required for high particle densities. On the downside the amplitudes of the particle oscillations  $c_{2n}$  are proportional to  $q$ , so higher values of  $q$  result in larger oscillations and more particles are lost. [24]

Figure 2.4 shows the ion density in a 3D Paul trap as function of the Mathieu parameters. The simulations are very well in accordance with the measurements from laser-induced fluorescence and show a maximum ion density at  $q = 0.5 - 0.6$  for  $a = 0$  [31].





### 3. Buffer Gas Cooling of Negative Ions

The use of buffer gas for the cooling of ion beams inside traps and ion guides is a widely used technique [28, 29, 30, 32]. Thereby the ions are surrounded by a light buffer gas (in most cases helium) and the ions lose energy in elastic collisions with the neutral gas atoms. They thermalize, meaning that they approach equilibrium conditions in the gas. In a simple approximation, the process can be understood as a damping of the particles' motion in all three spacial directions. In a trap, the cooled ion beam is reduced in both, position and momentum space and the cooled ions gather in the minimum of the trapping potential. At rare isotope facilities, buffer gas cooling inside an ion guide is used to reduce the emittance of the rare ion beam [28, 30]. [24, 33]

At most of these facilities, positive ions are used. As opposed to this, we have to deal with negatively charged atomic and molecular ions – a constraint given by the application of optical filtering for AMS. Negative ions are much more difficult to handle because they can easily be neutralized by collisional detachment. In order to avoid these losses, the energy in the CM frame of the collision must not exceed the electron affinity, which is the threshold for detachment. The particle's kinetic energy transforms into the CM frame like

$$E_{CM} = \frac{m_b}{m_i + m_b} E_{Lab} \quad (3.1)$$

with  $m_i$  and  $m_b$  being the masses of the ion and buffer gas atom, respectively [29].

Copper, for example, has an electron affinity of 1.24 eV (see table 1.1). With  $m_i=63$  and  $m_b=4$  the threshold for collisional detachment in helium is 20.8 eV kinetic ion energy in the laboratory frame. If the copper ions are decelerated electrostatically below 20.8 eV before entering the buffer gas filled volume, all losses due to collisional detachment are avoided. In the experiment the optimum injection energy for copper is above this threshold, at 50 eV, due to the competing mechanism of losses caused by the angular divergence of the beam (see section 5.4).

$E_{CM}$  is the maximum energy that can be transferred in one collision. The lighter the buffer gas (and the heavier the ion), the smaller is the energy transfer in one collision. A small energy transfer per collision is favorable for the injection as well as for the cooling process. Concerning the injection into the gas filled volume, a small buffer gas mass results in a higher threshold for collisional detachment and therefore in a larger acceptance of the device. Regarding the statistical cooling process, a higher buffer gas mass results in higher losses. Once an ion is thermalized it loses on average as much energy in collisions as it gains. The probability of losing a particle due to energy gain from a collision is higher for a larger buffer gas mass. It has been demonstrated that  $K^+$  ions can be cooled in He, less efficient in Ar and not at all in Kr [28].

In the following, two models for the simulation of buffer gas cooling are discussed. The

macroscopic approach introduces a viscous force that damps the ion motion, while the microscopic description models single ion-gas collisions.

### 3.1. Macroscopic Approach

When an ion moves through a gas, it polarizes the neutral gas atoms. The long-range interaction between ions and polarized gas atoms lets the gas act as a viscous medium. [33]

The viscous damping model introduces a force proportional and opposite to the ion velocity  $\vec{v}$

$$\vec{F}_{vis} = m \cdot \vec{a}_{vis} = -\delta \cdot m \cdot \vec{v} \quad (3.2)$$

with the damping coefficient  $\delta$

$$\delta = \frac{e}{m} \cdot \frac{1}{\mu} \cdot \frac{p}{T} \frac{T_n}{p_n} \quad (3.3)$$

where  $e$  is the elementary charge,  $m$  the ion mass,  $p$  and  $T$  the pressure and temperature of the buffer gas,  $p_n$  and  $T_n$  the normal pressure and temperature and  $\mu$  the reduced ion mobility. In the absence of other forces, such a linear damping term results in an exponential decay of the velocity with  $v(t) = e^{-\delta t} v_0$ . Ion mobilities can be found listed in the literature for various kinds of ions and gases. For known values of  $\mu$ , trapping times can be estimated [28].

For  $\text{Cl}^-$  ions in He, the reduced mobility is given in [34] as

$$\mu = 20.3 \frac{\text{cm}^2}{\text{Vs}} \quad (3.4)$$

for a vanishing electric field. The resulting damping coefficient is

$$\delta = 0.143 \frac{1}{\mu\text{s}} \quad (3.5)$$

at room temperature for a He pressure of 0.1 mbar. This value is used in the simulations described in section 3.3, scaled for different pressures of the buffer gas.

The damping model can easily be implemented in a SIMION simulation via an additional term in the ion acceleration. The current velocity and acceleration of the ion are internal SIMION variables. The damping term is added to the acceleration  $\vec{a}$ , as calculated by SIMION from the RF and guiding fields.

$$\vec{a}_{tot} = \vec{a} + \vec{a}_{vis} = \vec{a} - \delta \vec{v} \quad (3.6)$$

The model is based on the damping effect due to polarization, with the constant drift velocity following directly from the measured ion mobility. It is therefore a good description at low energy ( $< 1$  eV) and suitable for roughly estimating the residence time of the ions in the cooler [33]. In other aspects it is highly limited. Within the damping model the ions never thermalize with the gas, in fact their temperature approaches zero because their velocity continuously decreases. For further predictions and a better understanding of the buffer gas cooling, a more realistic model is needed.

## 3.2. Microscopic Approach

At high energies, in the MeV-range, the energy loss of ions in matter is dominated by electronic stopping. In the keV to eV range the dominating process is nuclear stopping, which can be understood as the energy loss due to elastic collisions (see figure 3.1). At energies below 1 eV, the polarization of the buffer gas has to be taken into account [33].

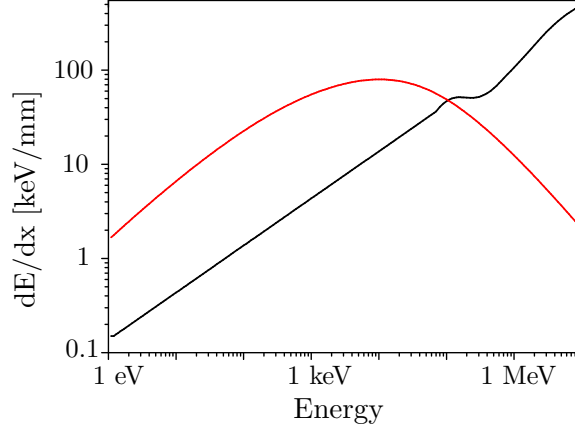


Figure 3.1.: Contribution of nuclear stopping (red) and electronic stopping (black) to the energy loss of a  $\text{Cl}^-$  ion in 0.001 mbar He. Data taken from SRIM [35].

Within the microscopic approach, the cooling in a buffer gas is described as elastic collisions between ion and gas atoms which are modeled as hard spheres. In every collision the ions lose energy until they are in equilibrium with the buffer gas and gather in the minimum of the trapping potential. In good approximation the collisional cross section equals the geometrical cross section derived from the Van der Waals radius of the buffer gas atom and the ionic radius of the ion [36]. For example, the radii of neutral helium [37] and negatively charged chlorine [38] are

$$\begin{aligned} r_{\text{He}} &= 140 \text{ pm} && \text{for He} \\ r_{\text{Cl}^-} &= 181 \text{ pm} && \text{for Cl}^- \end{aligned}$$

resulting in a geometrical cross section of

$$\sigma = (r_{\text{He}} + r_{\text{Cl}^-})^2 \pi = 3.24 \cdot 10^{-19} \text{ m}^2. \quad (3.7)$$

This value is used in the simulations described in section 3.3.

This microscopic picture can be implemented as a Monte Carlo routine embedded in a SIMION user program. Within the hard-sphere model, single elastic ion-gas collisions are modeled, assuming the background gas velocities to be randomly distributed according to a Maxwell-Boltzmann distribution. The probability of hitting a gas atom is calculated according to the buffer gas density, the geometrical cross section and the randomized gas velocities. In the absence of any forces, the ions approach the same temperature as the gas and their velocities become Maxwell distributed [36]. In the cooler the ions are constantly accelerated by the RF field, therefore the equilibrium temperature of the ions is above the buffer gas temperature.

### 3.3. Simulation of Buffer Gas in SIMION 8.1

SIMION [39] is a commercial charged particle optics simulation software. It calculates electric and magnetic fields by solving the Laplace equation using a finite elements method. Ions can be flown through an array, with the software calculating the particle trajectories. Via user programs, one can implement, for example, time-dependent fields and make changes to the particle's properties like its velocity or acceleration. I have implemented the viscous damping model and the collisional hard-sphere model for buffer gas cooling as SIMION user programs. The commented codes for both models and the geometry are attached in the appendix. The geometry for the simulation includes the whole electrode structure of the ILIAS cooler, made up of four RF electrodes and four guiding electrodes. They are surrounded by a tube, which is on ground potential. All electrodes are 800 mm in length. The guiding electrodes are slightly tilted in order to produce a longitudinal field gradient that provides a preferred direction for the thermalized ions towards the end of the cooler. If this guiding field is turned off, the ions get stuck within the damping model. Within the hard-sphere model the ion carries out a random walk, that ends once it reaches one of the cooler ends. It is assumed that the cooler is homogeneously filled with gas and that the mean gas velocity is zero. There is always one ion flying at a time, so the simulation does not encounter for space charge effects. The following settings were used for all simulations presented in this section.

Mass	Initial ion energy	GELEC	RF amplitude	RF frequency	Mathieu $q$
36 amu	50 eV	-50 V	200 V	2.6 MHz	0.42

Both simulations have been carried out for three different assumptions on the buffer gas pressure. It is only possible to measure the pressure at the gas inlet which is located in the center of the cooler. In this position 0.1 - 0.2 mbar is a typical working pressure. The pressure drops towards the ends of the cooler, resulting in a slightly smaller average. Unfortunately the exact pressure profile in the cooler is currently unknown. However, at least in the center of the cooler it is supposed to be close to the pressure measured at the gas inlet. In the simulation a homogeneous pressure distribution is assumed. Three different values were used in the simulation, 0.1 mbar, representing the upper limit for the case of a negligible drop towards the cooler ends and two smaller values, for the cases of a correspondingly greater drop.

#### Residence Times

Total residence times in the cooler are in the range of few ms. In the following table residence times at three different buffer gas pressures are listed for both models. Within the damping model, the same initial conditions always result in the same final state. The values and uncertainties given for the collisional model are the average and standard deviation over the residence times of 10 ions. Due to the random behavior, the resulting residence times are statistically spread. The mean free path between two collisions depends on the buffer gas pressure and the geometric cross-section:  $\lambda = \frac{kT}{p \cdot \sigma}$ .

Pressure [mbar]	Damping model	Collisional model	
	Residence time [ms]	Residence time [ms]	Mean free path [mm]
0.01	0.12	1.2(2)	13.19
0.05	4.64	5.7(8)	2.64
0.10	10.48	11(2)	1.32

#### Thermal Equilibrium

Within the collisional model the ions reach an equilibrium which is a trade-off between accelerating RF field and cooling through collisions. Then the kinetic energy fluctuates with a mean standard deviation of 0.09 eV around the mean kinetic energy of 0.08(2) eV (see figure 3.2). Once the ions reach equilibrium, they are confined to the trap center within a maximal distance of about 0.5 mm from the axis. The cooling time, meaning the time needed to reach the mean equilibrium energy, and the cooling length, meaning the distance traveled in the longitudinal direction within the cooling time, are listed in the following table for three ions in different helium pressures.

Pressure [mbar]	Collisional model		Damping model	
	Cooling time [μs]	Cooling length [mm]	Cooling time [μs]	Cooling length [mm]
0.01	320	700	>120	>800
0.05	150	90	47	186
0.10	100	50	22	92

For the collisional model, the cooling time is the characteristic parameter. Cooling lengths can vary, since the ion can change its direction of movement along the axis through scattering, moving back and forth in a random manner. When applying the damping model, the ions can never change their direction of movement along the z-axis. The energy decreases exponentially, never reaching an equilibrium state. At 0.01 mbar pressure the residence time of only 120 μs is not long enough for the energy to reach this level. In figure 3.4 the trajectories of the ions at 0.05 mbar and 0.1 mbar gas pressure are shown.

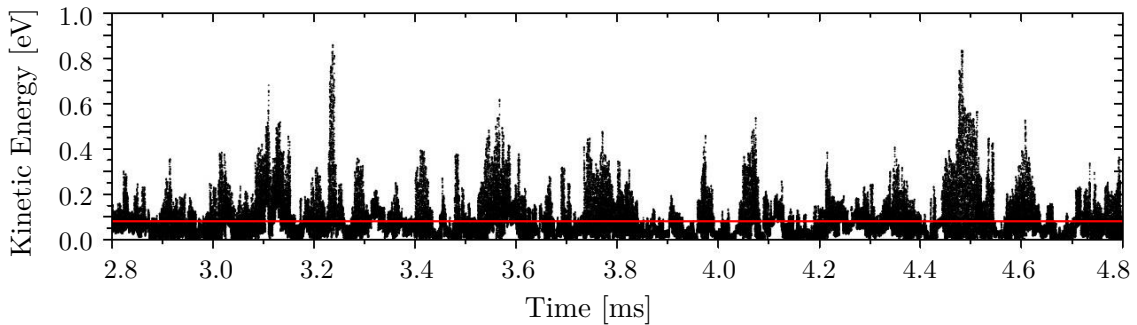


Figure 3.2.: Kinetic energy of a  $\text{Cl}^-$  ion in equilibrium with the buffer gas (0.05 mbar) during its last 2 ms in the cooler. In equilibrium the kinetic energy fluctuates around the mean kinetic energy of 0.08 eV (red).

### Comparison of the Models

Figure 3.3 demonstrates the decay in the ion's energy and energy spread. Cooling times are shorter with the collisional model than they are with the damping model. The collisional model is a more realistic description of the energy loss process in the energy range above 1 eV, therefore it probably gives a more accurate estimation on the cooling time. The damping model overestimates cooling times, since it does not describe properly the situation above 1 eV.

The predictions on the total residence time are very well in accord for buffer gas pressures of 0.05 mbar and 0.1 mbar, where the ions are in equilibrium with the gas most of the time. The damping model is much easier to implement and sufficient for giving a rough estimation on the total residence time. However, if one is interested in cooling times, equilibrium energy, energy spread or spacial distribution of the beam, there is no way around the more complicated collisional model.

The collisional model can be improved by using a realistic interaction potential that models the long-range interaction between ions and gas atoms instead of the simple hard-sphere model. It turns out that mobility data simulated with such a realistic interaction potential is in accord with experimental data, while the values obtained with the hard-sphere model differ by a factor of up to three. [33]

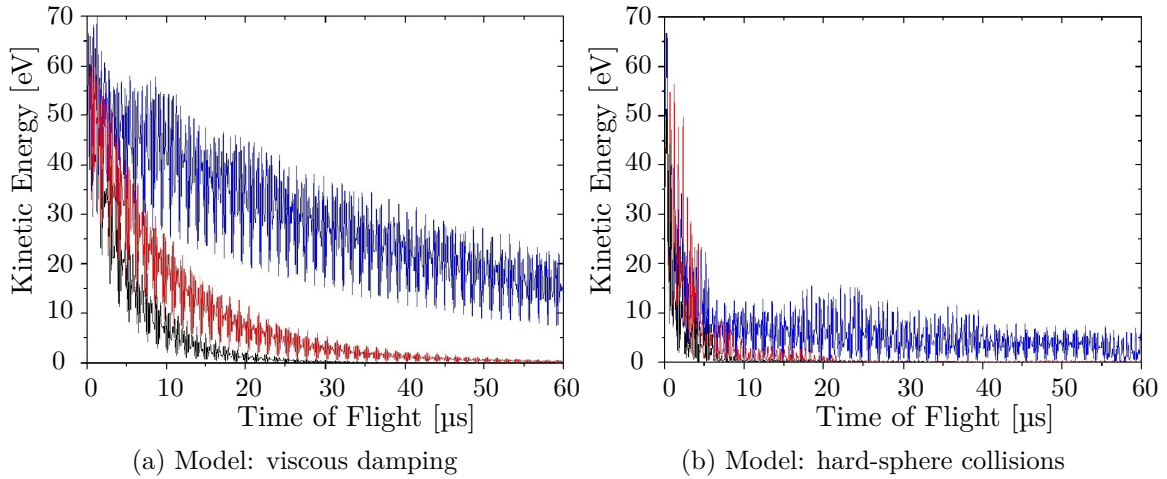
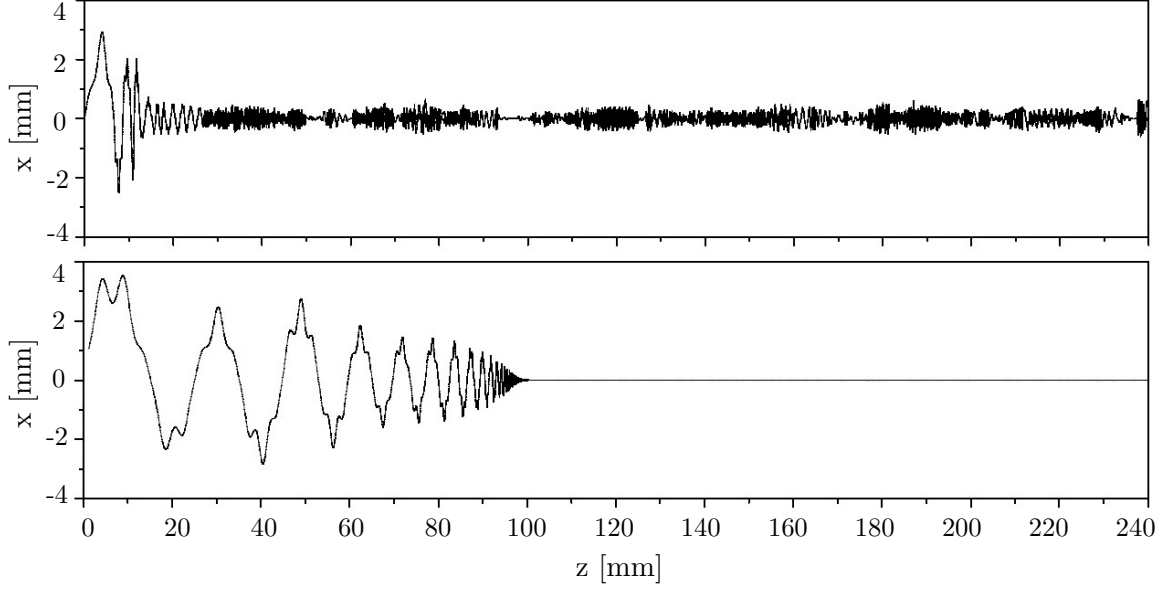
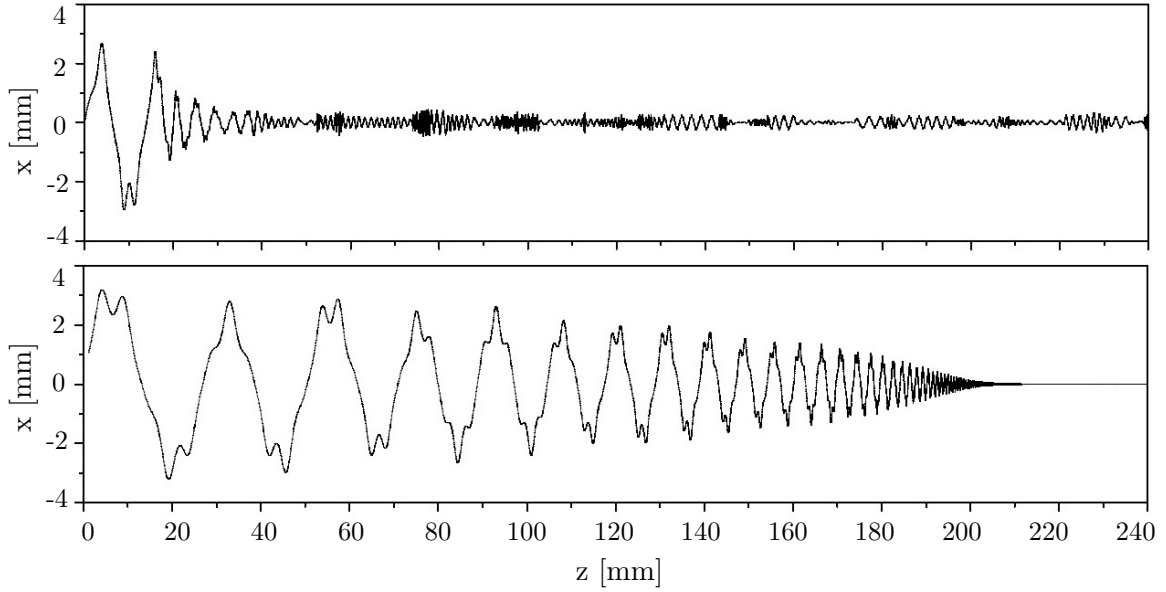


Figure 3.3.: Kinetic energy of a  $\text{Cl}^-$  ion as function of time of flight at 0.1 mbar (black) 0.05 mbar (red) and 0.01 mbar (blue) He pressure. Cooling times are shorter with the collisional model than they are with the damping model. Energy and energy spread are reduced. The initial ion energy is 50 eV.



(a) 0.1 mbar He, top: hard-sphere collisions, bottom: viscous damping



(b) 0.05 mbar He, top: hard-sphere collisions, bottom: viscous damping

Figure 3.4.: Trajectories of  $\text{Cl}^-$  in the ILIAS cooler at different buffer gas pressures. The longitudinal axis is denoted  $z$ . When the ions are in thermal equilibrium (collisional model), they are confined to the axis within a radius of about 0.5 mm.



## 4. ILIAS Ion Beam Cooler

### 4.1. General Setup

In the cooler the ions are first decelerated electrostatically and then further cooled by collisions with the buffer gas. Electrostatic deceleration is realized by setting the cooler on a potential slightly below the source potential. After electrostatic deceleration the ions enter the gas-filled cooler with an injection energy of some 10 eV where they are captured by the RF field and cooled down to about 0.1 eV by the buffer gas. The ion beam cooler has two purposes:

- The ion-laser interaction time is extended to the ms range. The depletion of a state by laser photodetachment follows an exponential decay law [9]

$$N(t) = N_0 \cdot e^{-\sigma\phi t} \quad (4.1)$$

with  $t$  [s] the interaction time,  $\sigma$  [cm<sup>2</sup>] the cross section for laser photodetachment and  $\phi$  [cm<sup>-2</sup>s<sup>-1</sup>] the photon flux. Since the photon flux is limited by the laser power available, the interaction time has to be extended in order to reach a higher depletion. This can either be done by slowing down the keV ions or by realizing a long interaction region. The latter is definitively not feasible, since it would require an ion-laser overlap of about 1 km, therefore the slowing down of the ions seems to be the natural choice.

- Excited molecular states such as vibrations and excitations are disturbing because they lower the threshold for laser photodetachment. Molecular ions that are produced in a cesium sputter source usually also populate excited states. A smaller detachment energy results in beam losses of the ion species of interest due to collisional detachment and laser photodetachment. It is not guaranteed any more that the chosen laser wavelength affects only the unwanted isobar. With the ion beam cooler, excited states should be cooled down to the ground state by elastic collisions with the buffer gas; however, the process of cooling has to be faster than the depletion of the excited states by laser photodetachment in order to reduce the losses significantly. The cooling of excited states in negatively charged molecular ions by buffer gas cooling has never been investigated before and it is therefore in question if excited states can be cooled to the ground state at all.

#### 4.1.1. Injection

The deceleration section is composed of several electrodes that provide a smooth field gradient and focus the beam: the ground electrode on lab ground, the deceleration electrodes named ‘high’ and ‘low’ lens and the cooler aperture on cooler high voltage. The ground electrode is a tube with an inner diameter of 20 mm. Both injection lenses are flat aperture lenses with the diameter of their openings being 20 mm for the ‘high’ lens

(INJHI) and 10 mm for the ‘low’ lens (EXTLO). The power supplies for the lenses have positive polarity and are placed inside the safety cage with their ground being on cooler high voltage. The cooler aperture has a diameter of 3 mm and closes the cooler tube that holds the electrode structure. Figure 4.1 shows a schematic drawing of the cooler section.

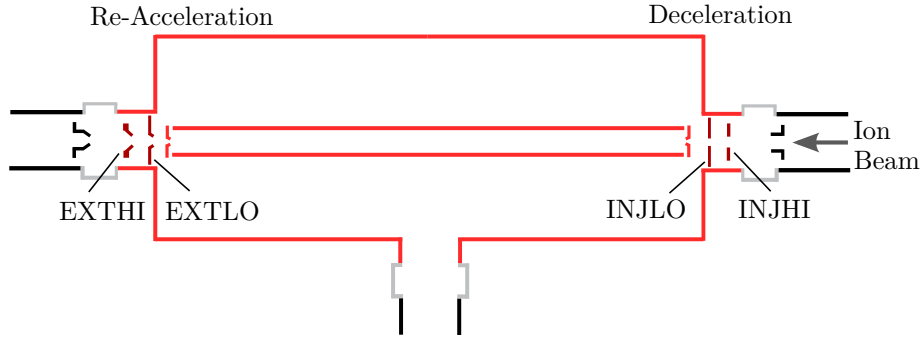


Figure 4.1.: Schematic drawing of the cooler section (not to scale). The colors emphasize that the electrodes and beamline sections are on different electrostatic potentials: cooler HV (light red), deceleration and re-acceleration potentials (dark red), lab ground (black) and insulators (gray).

The term injection energy in the context of the ion cooler refers to the ion energy after electrostatic deceleration due to the cooler high voltage. It is determined by the potential difference between ion source and the cooler. However, the kinetic energy of the (uncooled) ions on the cooler axis is determined by the sum of the cooler high voltage and the on-axis potential caused by the guiding electrodes. The ground of the guiding electrodes’ power supply is on cooler high voltage, as it is for the lenses. Both power supplies, RFQ.HV and GELEC have negative polarity, therefore the absolute values add up. An injection energy as low as possible is of advantage for two reasons:

- Losses due to collisional cooling inside the cooler are reduced when lowering the injection energy. There is no more improvement when the ion’s kinetic energy on cooler axis is smaller than the threshold for collisional detachment.
- The time required to cool the ions is smaller for a lower injection energy. This results in a longer ion-laser interaction time because the ions are sooner confined close to the axis, where the photon flux is greatest.

On the downside, when the beam is decelerated, the velocity component in the direction of the beam’s propagation is reduced, while the others stay unaffected, resulting in an increased angular divergence of the beam. The injection energy is therefore a quantity that has to be tuned and is a compromise between losses due to angular divergence and collisional losses.

### 4.1.2. Transport Through Cooler

The cooler in the narrower sense is a metal tube, 810 mm in length with an inner diameter of 40 mm. The electrode structure, consisting of the four RF rods and the four guiding electrodes, is placed inside the cooler tube and held in place by six ceramic spacers, which are equally distributed over the full length of 800 mm. The guiding electrodes are tilted

by  $0.036^\circ$  and produce a field gradient that gives the particles a preferred direction in the gas-filled volume (see section 4.4). The RF rods have a circular cross section of  $r=5.00$  mm radius and the inscribed circle has a radius of  $r_0=4.37$  mm (see figure 4.2a). When using circular instead of hyperbolic rods, the ratio  $r/r_0$  has to be chosen such that a quadrupole field is best approximated. According to Denison [27]  $r=1.1468r_0$  is the best approximation for a quadrupole with cylindrical electrodes in a grounded cylindrical housing of  $3.54r_0$ . For that specific ratio the 12-pole term vanishes and the quadrupole term dominates the field in the trap center. In the case of the ILIAS cooler, the cooler tube and guiding electrodes also change the field configuration. The ratio of  $r=1.144r_0$  slightly differs from the theoretically best value for the circular rods geometry.

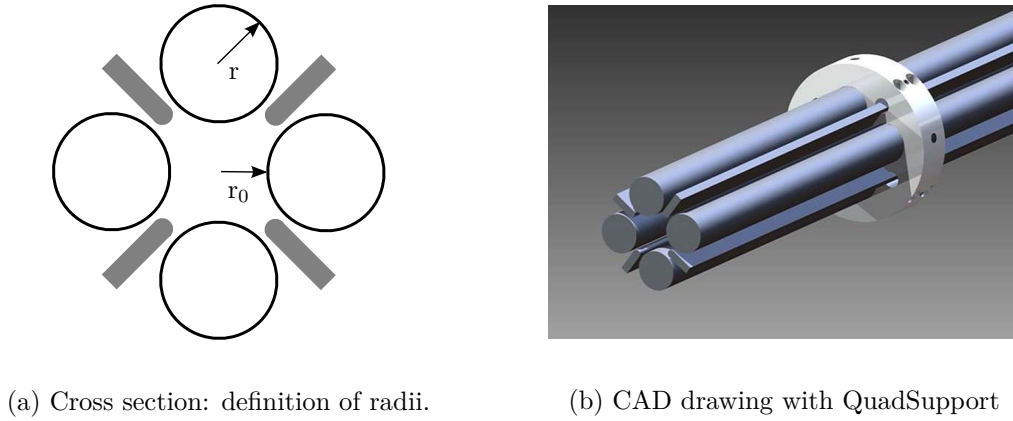


Figure 4.2.: Electrode Structure

As shown in section 3.3, the buffer gas cooling reduces the ion energy to about 0.1 eV. The interaction time is extended due to the smaller velocity of the ions and because the amplitudes of the ions' oscillations in the ion guide is reduced, resulting in a better ion-laser overlap. The cooling of the ion beam reduces the beam's emittance. The beam properties after the re-acceleration are therefore better than the initial properties coming from ion production in the source.

#### 4.1.3. Extraction

In the cooling process all information of the injection into the cooler is lost because energy and momentum are reduced and statistically distributed over all spacial directions through the elastic collisions with the buffer gas. Lunney et al. humorously describe this effect as 'brainwashing' [40]. The extraction has to be carefully designed, since it can be regarded as the ions' starting point for the rest of the beamline. In particular, the extraction defines the ion beam's properties for injection into the accelerator of the AMS facility.

The energy of the extracted beam equals the ion energy after the source, minus the initial ion energy in the quadrupole, which is lost in the cooling process.

The setup of the re-acceleration section is similar to the deceleration: a 3 mm diameter cooler aperture closing the cooler tube, two acceleration electrodes (EXTLO and EXTHI) and the ground electrode. In the original design, the ground electrode and extraction high lens had a conical shape, while the low lens and the cooler aperture looked the same as

on the injection side. This was modified later as described in section 4.5.2. Simulations of the injection and extraction are presented in section 4.5.3.

## 4.2. Electronics Setup

### 4.2.1. Radio Frequency Setup

As already explained in section 2.1.3, the quadrupole's storing capability of space charge is limited by the depth of the pseudo potential well (see equation 2.19). Since the Mathieu parameter  $q$  is limited by the stability of the particle trajectories, the depth of the well can only be extended by increasing the RF amplitude. For the same value of the Mathieu parameter  $q$ , the voltage should be as high as possible in order to maximize transmission. The RF amplitude is limited by the radio frequency setup and the ability of the mechanical parts to cope with the voltage.

Figure 4.3 shows a sketch of the RF setup. A function generator (Stanford Research Systems DS345) provides a sine wave signal with an amplitude of typically 0.2 V. This signal is amplified by a factor of up to 200 by a 400 W power amplifier (E&A 1040 L). The output feeds the primary circuit of a ferrite transformer. On the secondary side, two circuits are coiled in inverse direction such that there is a  $180^\circ$  phase shift between the secondary circuits. Each circuit drives two opposite rods of the quadrupole. The RF amplitudes are measured on the secondary side (zero to peak). The whole setup is floating on cooler high voltage.

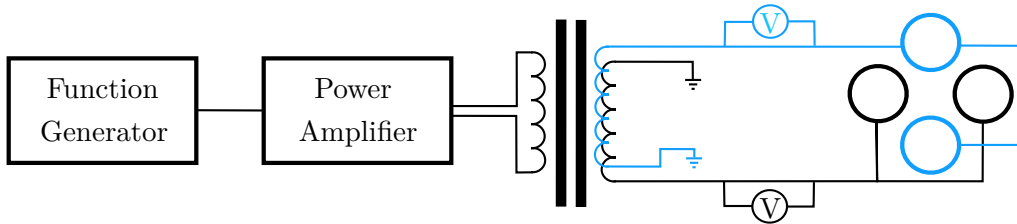


Figure 4.3.: Radio frequency setup.

With this setup a lot of power is reflected and goes back to the amplifier. To a certain degree the amplifier can handle it but if the amplitude and thereby the reflected power is too high, it shuts down. Moreover, at high frequencies, the amplitude is strongly limited by the amplifier. According to equation 2.12, a higher frequency requires a higher amplitude to keep  $q$  constant. Unfortunately, the amplitude falls drastically when going towards higher frequencies due to the frequency response characteristic of the amplifier. Therefore the RF amplitude is limited with this setup, especially for low masses.

A new RF setup is currently being developed and first tests look promising. The secondary side consists of two resonant circuits, tuned to the capacity of the quadrupole. The advantage is that the energy is stored in the circuit and less power is reflected back to the amplifier. Furthermore, the resonant circuit amplifies if it is properly tuned. Higher amplitudes can be obtained, in comparison with the setup described above. Therefore a smaller (200 W) amplifier is sufficient which lowers the costs for the RF setup. A disadvantage is that the capacity and inductivity of the circuits have to be tuned for an ion mass according to the corresponding frequency and amplitude.

### 4.2.2. Electronics Setup of the Guiding Electrodes

It is necessary to install a resistor and a capacitor between the guiding electrodes and cooler ground. The capacitor filters out any AC noise from the RF setup. The resistor allows the guiding electrodes to discharge when they get hit by the ion beam. The power supply has negative polarity and can be damaged when the guiding electrodes charge up negatively. The lenses do not suffer from this problem because the power supplies have positive polarity and the negative charges from the ion beam can discharge through the power supply.

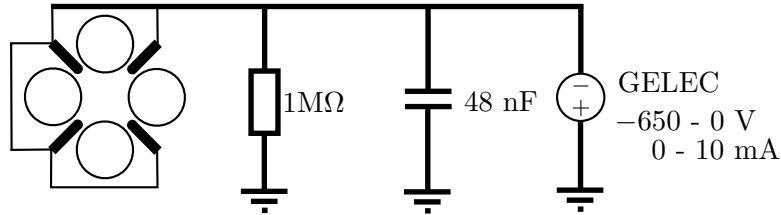


Figure 4.4.: Electronics setup of the guiding electrodes.

## 4.3. Vacuum

Due to the large pressure gradient from 0.1 mbar in the cooler tube to  $10^{-7}$  mbar in the beamline, several stages of differential pumping along with strong vacuum pumps are required. Special attention has to be paid to the deceleration and re-acceleration sections. Here the particles have kinetic energies considerably above threshold for collisional detachment. Buffer gas leaking from the cooler tube into the beamline has to be avoided otherwise the beam might suffer from losses due to collisional detachment.

Figure 4.5 shows a schematic drawing of the cooler section with attention on the buffer gas and residual gas pressure. A gas bottle feeds the gas supply line, which is under a pressure of 2 bar in order to keep the pressure in the following gas inlet line constant. The pressure in the gas inlet line is regulated manually via a needle valve. A pirani gauge (RFQ.GIN10) measures the pressure in the gas inlet line which is typically around 0.1 - 0.2 mbar for He. It is mounted close to the gas inlet in the middle of the cooler tube. The pressure in the tube cannot be measured directly. However, the gas inlet is rather large with a diameter of about 10 mm, so the pressure measured in the gas inlet line gives a good measure of the pressure in the cooler tube. The cooler tube and cooler apertures are the first stage of differential pumping. Buffer gas can exit the cooler tube through the 3 mm aperture and additional pumping holes at both ends of the cooler tube. The cooler section surrounding the cooler tube is pumped by a 1250 l/s turbomolecular pump. The pressure in this section is about  $1 \times 10^{-5}$  mbar, measured by an ionization vacuum gauge in the cooler vessel. The lenses are a further barrier for differential pumping, separating the cooler section from the outer beamline sections. Two 685 l/s turbomolecular pumps before and after the cooler section provide the necessary pumping power to handle the buffer gas leaking through the lenses. The vacuum is also measured in the beamline sections before and after the cooler by ionization vacuum gauges.

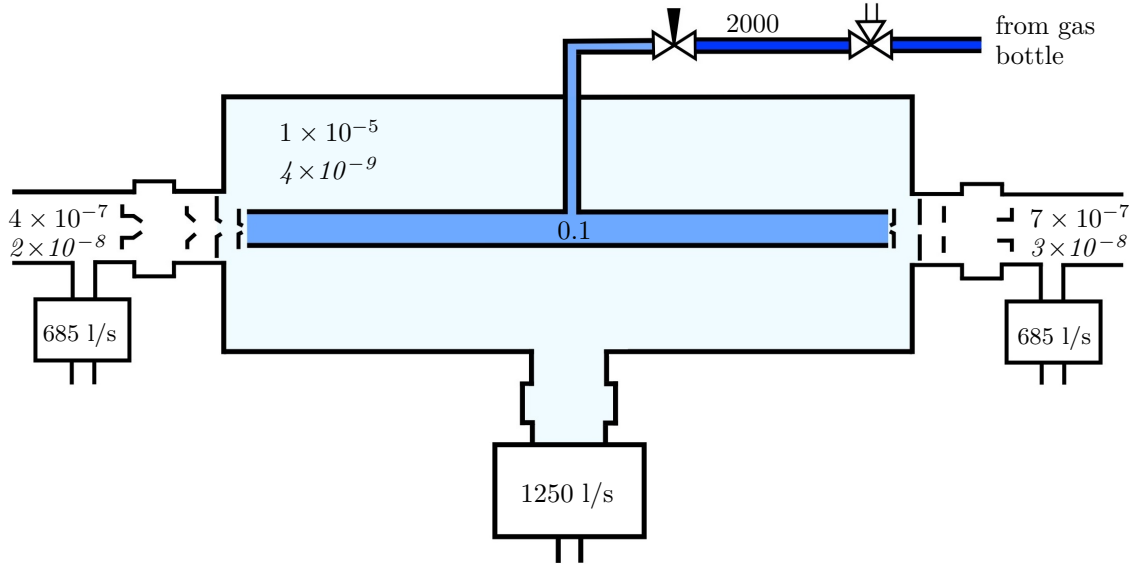


Figure 4.5.: Schematic drawing of the cooler (not to scale). All pressure values are in mbar. Values for vacuum without buffer gas are given in italics.

When the cooler voltage is turned on, the gas supply line has to be evacuated or be under atmospheric pressure. An intermediate gas pressure (e.g. when pumping the gas supply line) leads to discharges inside the gas supply line or the pump. Up to now only He has been used as a buffer gas.

#### 4.4. Guiding Electrodes

The purpose of the guiding electrodes is to produce an axial field gradient along the whole length of the cooler in order to give the ions a preferred direction when diffusing in the buffer gas. The voltage set on the guiding electrodes defines the accelerating field along the longitudinal axis and thereby controls the ions' residence time inside the cooler.

All four guiding electrodes are 800 mm long, flat bars made from stainless steel. They are placed symmetrically between the RF rods and are held in place by six ceramic spacers. The voltage on the guiding electrodes is negative with respect to the cooler HV, in order not to attract the negative ions. At the injection side the guiding electrodes are placed closer to the axis than at the extraction side. The shift in position of 0.5 mm between the two ends of the cooler corresponds to a tilt of  $0.036^\circ$ . A typical on-axis potential difference between injection and extraction side is in the order of few Volts. For negative ions the axial field gradient represents an accelerating field towards the extraction side.

The following table shows the electric potential inside the cooler for various settings of the guiding electrodes relative to cooler ground. The values were determined within a SIMION simulation of the cooler (for geometry see appendix A.1). The cross section of the cooler simulation is shown in figure 4.7. The potentials are read out on-axis (meaning the center of the cross section) on both ends of the cooler relative to cooler ground with the RF electrodes set to zero. All values are directly proportional to the voltage applied to the guiding electrodes. The proportionality factor, determined through linear regression, is also given in the table.

GELEC [V]	Injection [V]	Extraction [V]	Potential difference [V]
-20	-3.58	-2.41	1.17
-40	-7.18	-4.82	2.36
-60	-10.75	-7.23	3.52
-80	-14.35	-9.64	4.71
-100	-17.93	-12.05	5.88
lin regression	$0.1793(1) \cdot \text{GELEC}$	$0.1205(1) \cdot \text{GELEC}$	$0.0588(1) \cdot \text{GELEC}$

As mentioned before, the electrode structure is held in place by ceramic spacers. These spacers (QuadSupport) are made from Macor<sup>®</sup>, a machinable ceramic which has very good insulating properties.

#### 4.4.1. Original Design

In the original design, the guiding electrodes were fixed completely only at the ends with the outermost spacers, the QuadSupportApertures (see figure 4.9a). The four inner QuadSupport ceramics only clipped the guiding electrodes, leaving some freedom in the radial direction (see figure 4.6a).

In operation it turned out that the transmitted ion current dropped dramatically when the voltage on the guiding electrodes (GELEC) was turned on. Having the design described above in mind, it seemed natural to investigate the consequences of a displacement of the guiding electrodes. A SIMION simulation with displaced guiding electrodes showed that an asymmetric misalignment would indeed produce a steering effect that leads to beam losses (see figure 4.8).

Finally, the examination of the electrode structure during the maintenance of the cooler confirmed the assumption of a steering effect. The first ceramic after the QuadSupportAperture at the injection side showed heavy asymmetric beam deposits (see figure 4.6a). The guiding electrodes were displaced by up to 2 mm in some places. The electrodes obviously did not have enough dimensional stability to be held in place by the QuadSupport ceramics alone.

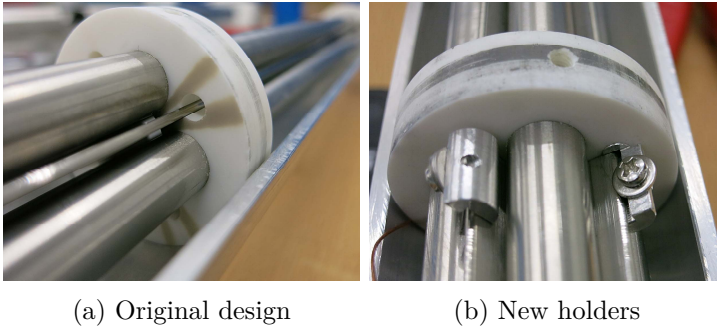


Figure 4.6.: Electrode Structure with QuadSupport

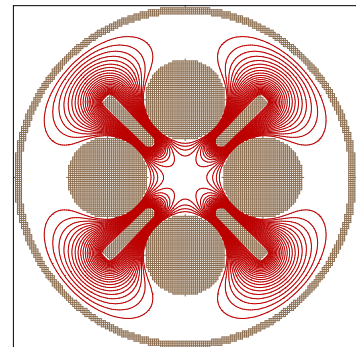


Figure 4.7.: SIMION simulation: equipotential contours.

#### 4.4.2. Modification

In order to correct for the displacement, additional holders were mounted. These holders are aluminum pins, fitting the already existing holes in the ceramics. The guiding electrodes are now clamped to these pins by a screw and a washer at every QuadSupport ceramic (see figure 4.6b). Considering the dimensional stability of the material and the alignment procedure (using pliers and a slide gauge), the overall accuracy of the guiding electrodes' position is  $\pm 0.05$  mm. Additionally, the new holders are also used for the electric contacting of the guiding electrodes.

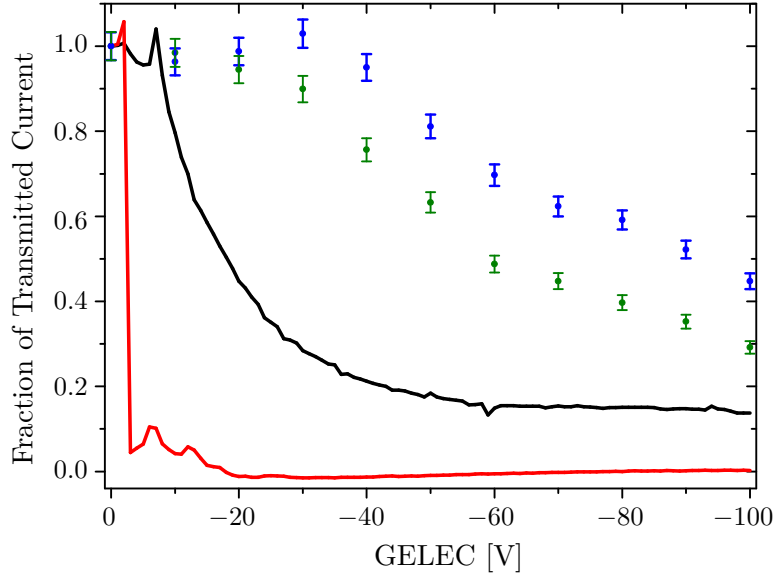


Figure 4.8.: Comparison of simulated and experimental data on the transmitted  $^{12}\text{C}^-$  current as a function of guiding electrode voltage without buffer gas. All currents are normalized to the current at  $\text{GELEC}=0$  V. During the scan of the guiding electrodes with the original design (red) and the modified holders (black) the extracted current was measured in FC 2. The data points are from a SIMION simulation. For each point 10000 ions of 100 eV were flown at an RF amplitude of 115 V and RF frequency of 3 MHz, which corresponds to  $q = 0.55$ . Blue data points correspond to the perfect geometry while the green data points were simulated with a geometry where two neighboring guiding electrodes are displaced radially by 1 mm, one towards the center, the other one away from the center. The new holders were crucial for enabling a beam transmission with the guiding electrodes turned on because a misalignment of the guiding electrodes increases beam losses.

The results of this modification can be deduced from figure 4.8, where the ion beam current in FC 2 is plotted as a function of guiding electrode voltage. The red curve gives the situation before and the black curve after the modification. Without the additional holders, the current dropped by 95% at  $\text{GELEC}=2$  V and basically vanished for  $\text{GELEC}>20$  V. With the new design it also decreases, but only gradually, never dropping below 15% of the initial value. Both scans were done with a  $^{12}\text{C}^-$  beam of 23 keV initial ion energy, without buffer gas. The data points in blue come from a simulation and represent the ideal case. Even though the geometry is perfect, turning on of the guiding electrodes leads to a certain beam loss. The new holders are a big improvement compared to the original design, where no beam could be extracted when using the guiding electrodes.

Figure 4.8 demonstrates the importance of an almost perfect geometry, but represents in no way any transmission in real experiments. The above considerations and measurements were done in the absence of any buffer gas. With buffer gas, ion losses along the transport through the quadrupole are further reduced due to the cooling effect.

## 4.5. Injection and Extraction

As already mentioned before, information of the injection is lost in the cooling process and the three stages of injection of ions into the cooler, transport through the cooler and extraction from the cooler can be considered completely independent. This is of interest because it means that there is no need for a simulation of the whole system, which would require a lot of computational power and would be as complicated to tune as the real system. For the optimization of the injection and extraction geometry it is sufficient to model only a small section of the cooler.

### 4.5.1. Original Design

In the original design, the QuadSupportApertures held the electrode structure at both cooler ends. These ceramic spacers had an aperture with a diameter of 3 mm and completely surrounded all eight electrodes so that their position was fixed (see figure 4.9a). A flat metal aperture, also with a 3 mm hole, closed the cooler tube. This cooler aperture was not connected to a power supply, but directly screwed to the tube (see figure 4.11a). It was therefore always on cooler potential. Both apertures acted as a barrier for the gas and were supposed to minimize buffer gas leaking into the beamline. The diameter of the apertures was a compromise between a minimum of gas leaking and maximum ion and laser beam transmission.

The cooler tube is about 10 mm longer than the electrode structure, which in the original setup resulted in a gap of 5 mm between the QuadSupportApertures and the flat cooler apertures. There were four 5×5 mm openings at both ends of the cooler tube, so that the volume between the apertures was not only pumped through the cooler aperture, but also sideways through these pumping holes.

The original design suffered from several problems and there was room for improvements.

- **Charging**

The QuadSupportApertures could charge up when getting hit by the ion beam. Beam deposits clearly showed that this happened. Since Macor is a very good insulator, the stored surface charge can get significant. Such a surface charge can lead to a steering effect or block the beam completely. Especially at the extraction side, where the ions have kinetic energies in the meV range, the beam is very sensitive and any field distortion can prevent the ions from exiting the cooler.

- **Gap**

Between the cooler aperture and the electrode structure there was a gap of 5 mm where only the fringe fields of the RF and guiding electrodes acted on the ions.

At the injection side, the angular distribution of the beam increases as the ions are decelerated. It would be more favorable to have the restoring force of the RF field capturing the ions right after they enter the cooler tube. Furthermore, it is undesirable

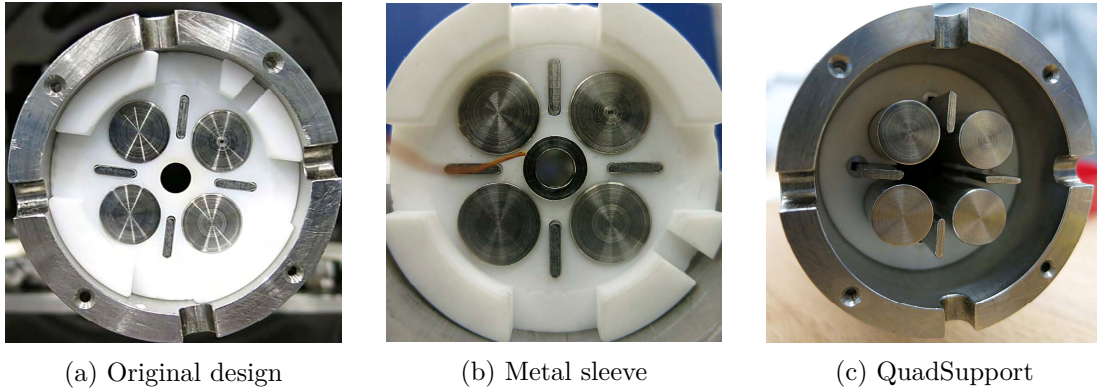


Figure 4.9.: Cooler end with electrode structure and ceramic spacer at different stages of development. (a) Original design with QuadSupportAperture. (b) The center of the ceramic spacer is covered by the metal sleeve. (c) The QuadSupport ceramic does not cover the electrode structure in the center. Here the cooler tube still has the  $5 \times 5$  mm pumping holes, which were later enlarged (see figure 4.11c).

for the focusing of the beam to have two apertures of the same diameter behind each other.

At the extraction side, the ions are accelerated towards the aperture by the potential difference between cooler ground and the on-axis potential inside the electrode structure, defined by the guiding electrodes. This potential difference is typically in the order of 5 - 10 V. Even though there were holes for pumping the gap, there could still be a considerable amount of gas in the gap. In most cases, the ions do not gain enough energy to suffer from collisional detachment inside the gap, but since the restoring RF force is missing, the presence of the gas will lower the beam quality due to energy and angular straggling. It is therefore also at the extraction side better to eliminate the gap.

- **Diagnostics**

A problem with the original design was that there were no diagnostic elements in the whole cooler section. Especially during the development of the cooler it is important to find out where the beam losses take place. The only possibility for diagnostic was to connect all electrodes (RF and guiding electrodes) to an amplifier. This procedure provides a measure for the beam current injected into the cooler, but of course the cooler itself can not be used at the same time.

#### 4.5.2. Modifications

All modifications on the cooler system were done in a way that the original state could have been easily restored.

- **Spacers**

In order to prevent the QuadSupportApertures from charging, metal sleeves were made that covered the ceramic in the direction of the incoming beam (see figure 4.9b). Via a Kapton<sup>®</sup> covered wire and a feedthrough, the sleeves could either be connected to a low noise amplifier or be put on cooler ground by shorting them with the cooler beamline section. When connected to the amplifier (Stanford Research Systems SR570)

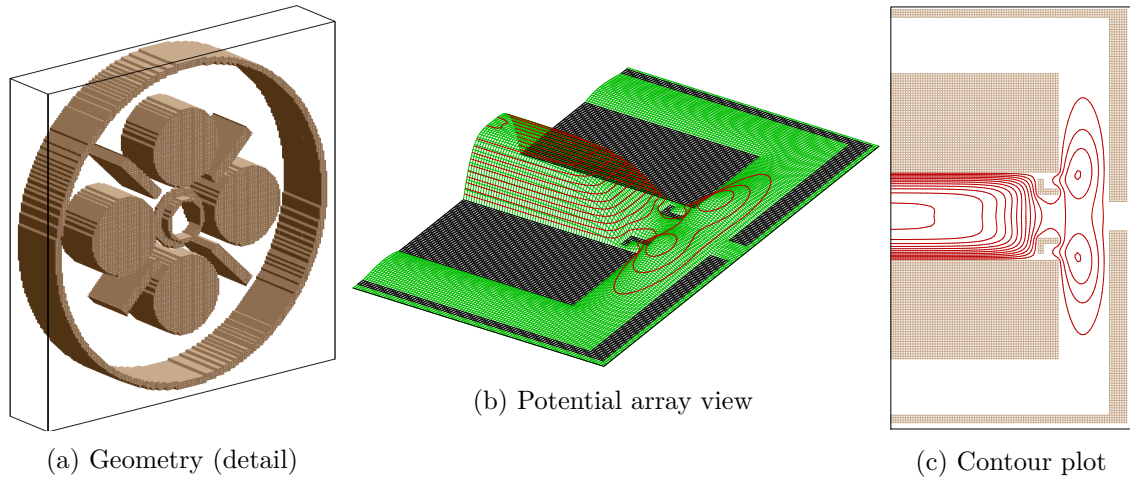


Figure 4.10.: Simulation of the extraction with metal sleeve.  $GELEC = -50$  V,  $Rf$  amplitude  $= 0$  V. A small potential well (0.5 V) appears between the extraction sleeve and the aperture.

an additional positive or negative bias voltage between  $-5$  V and  $5$  V could be applied. But most important, the ion beam current hitting the sleeves could be measured. Thus the metal sleeves acted as important diagnostic tools.

During the assembling of the cooler, the ceramic spacer at the extraction side broke. It was replaced by a QuadSupportAperture made from Teflon because it is easier and faster to machine. Unfortunately the properties of Teflon were not satisfying: it seemed to collect space charge and produced an offset on the read-out of the sleeve that changed on a time scale of hours. This emphasizes the importance of a proper choice of materials for elements inside the cooler, especially those close to the beam.

The fact that the cooled ion beam could be measured on the extraction sleeve, but could not be extracted from the cooler, gave rise to a further development. Later on it turned out, that a bad contacting of the low lens at the extraction side also contributed to the malfunction of the extraction. A simulation of the extraction region showed that the extraction sleeve creates a potential well between the sleeve and the cooler aperture. The simulation including the last 30 mm of the cooler tube, RF rods, guiding electrodes, the sleeve and the cooler aperture, is shown in figure 4.10. When the guiding electrodes are set to  $GELEC = -50$  V, this potential barrier is about 0.5 V high. The ions are accelerated when traversing the potential difference from inside the cooler to cooler ground and are therefore not disturbed by the sleeve. At the injection side the field configuration is similar, but the situation is not critical at all, since the ions are not cooled. In addition to the potential well, also surface charges on the spacer can lead to a distraction of the beam. Even if the metal sleeve prevents the area it covers from charging, charges could still accumulate on the surrounding area.

In order to avoid any possibility of a potential well or accumulated surface charges, the QuadSupportApertures with the metal sleeves were removed. They were finally replaced by QuadSupports with holders for the guiding electrodes, analogous to the four spacers along the electrode structure, on both, the injection and the extraction side. The new QuadSupports do not cover the electrodes in the center (see figure 4.9c).

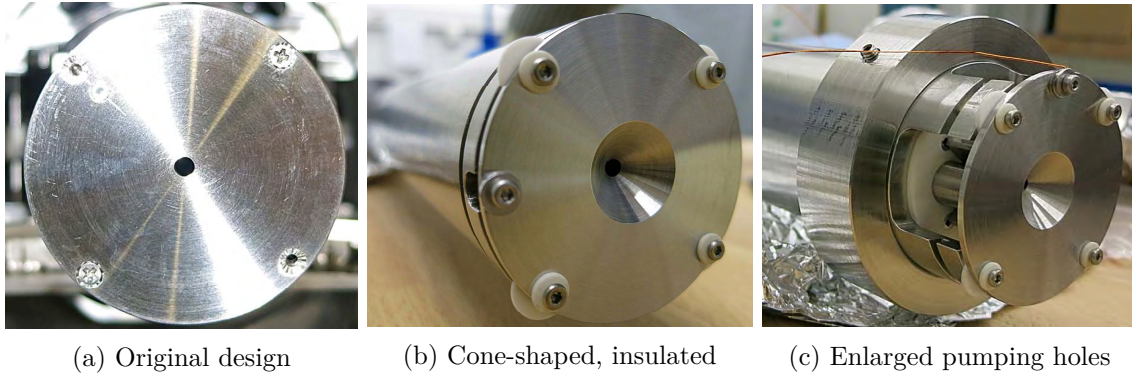


Figure 4.11.: Cooler aperture (3 mm opening) at different stages of development. (a) The originally flat aperture was directly screwed to the cooler tube. (b) The cone-shaped aperture is insulated by 1 mm ceramic spacers, resulting in a 1 mm pumping gap in addition to the original pumping holes. (c) The enlarged pumping holes can be closed by a slidable shell.

- **Apertures**

As discussed above, the gap between the cooler aperture and the electrode structure has to be avoided. Therefore the flat apertures (see figure 4.11a) were exchanged for cone-shaped ones (see figure 4.11b). The diameter of the openings is still 3 mm, but the cone tips lie in the same plane with the beginning and ending of the electrode structure. At the injection side, the beam can now be focused to the beginning of the electrode structure and the ions experience the restoring RF force right when they enter the cooler through the aperture. At the extraction side, the beam quality not only benefits from the elimination of the gap, as explained above: the cone shape also has a focusing effect that improves the ion optics of the re-acceleration.

Besides the change in shape, the mounting of the apertures differs from the original design. The apertures on both cooler ends are now electrically insulated from the cooler tube by ceramic spacers, which are 1 mm thick. The ion current hitting the apertures can be read out via a low noise amplifier, providing a further diagnostic tool. The corresponding read-out parameters are referred to as INJ.AP and EXT.AP for the aperture at the injection and extraction side, respectively.

- **Extraction**

Besides the aperture, the first lens (EXTLO) was modified. A SIMION simulation showed that when going to a conical shape rather than a flat aperture lens, the effective cross section of the lens opening can be reduced while maintaining similar ion optical properties. The low lenses are a main barrier for the differential pumping scheme and seal up towards the beamline tube. A smaller cross section of the lens opening is advantageous since the gas leaking into the beamline from the cooler section is equally reduced. The simulation in figure 4.14 includes the latest design of the extraction lenses and apertures.

- **Pumping**

In the original design, the buffer gas could exit the cooler tube on both ends through the 3 mm cooler aperture and four pumping holes of about  $5 \times 5$  mm, carved out from the cooler tube (see figure 4.9a). The pumping holes are meant to reduce the pressure in the volume between cooler aperture and QuadSupportAperture and thereby reduce

the leaking of buffer gas from the aperture towards the beamline. This is necessary because any residual gas in the deceleration and re-acceleration section can lead to beam losses due to collisional detachment.

With the insulated aperture, a 1 mm gap between cooler tube and cooler aperture was introduced (see figure 4.11b). This gap has the same effect as the pumping holes and increases the pumping of the cooler ends towards the sides. In order to further reduce the buffer gas pressure at the cooler ends, the pumping holes were enlarged to about  $10 \times 15$  mm. In the latest modification of the cooler a slidable shell was pulled over the cooler tube, making the size of the holes variable (see figure 4.11c).

### 4.5.3. Simulation of Deceleration and Re-acceleration

The redesign of the cooler apertures and extraction lens was accompanied by SIMION simulations that motivated the new design. The final design was chosen after comparing various simulations with different geometries. Here only the final design that represents the cooler in its current state is discussed.

The simulations of the deceleration and re-acceleration sections (figures 4.12 and 4.14, respectively), include an extended ground electrode, the high and low lens, the cooler aperture and a short section of the cooler tube without the electrode structure. Also the beamline surrounding the electrodes is included. The insulator that separates the cooler beamline section on cooler HV, from the beamline on lab ground, is modeled by a gap ('non-electrode'). In both simulations 100 particles of mass 63 and charge  $q = -1e$  are flown.

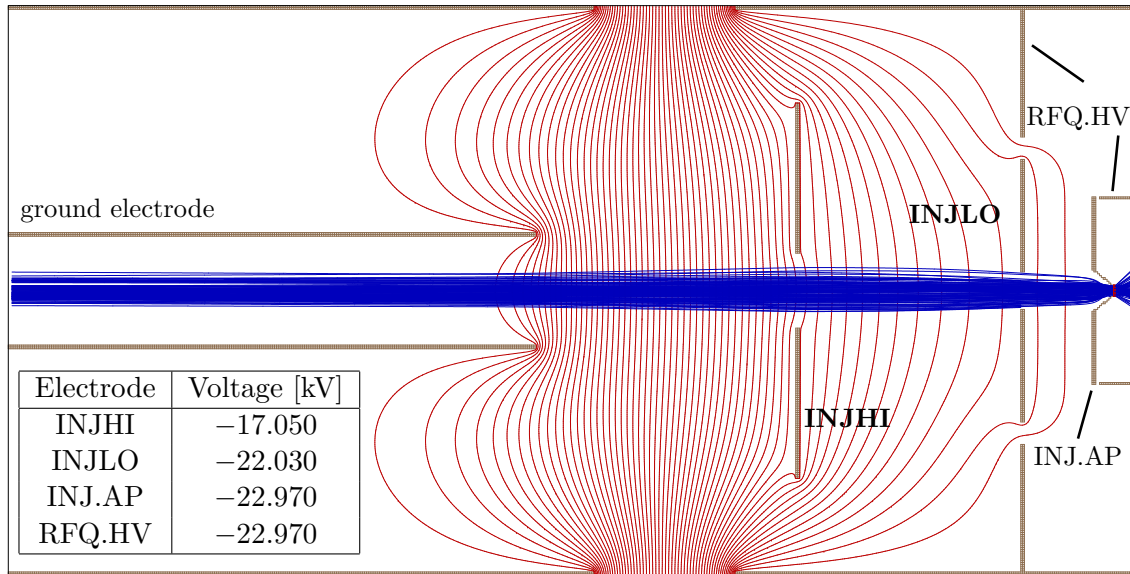


Figure 4.12.: Simulation of the deceleration section with equipotential contours (red) and ion trajectories (blue). The voltages on the electrodes relative to lab ground are listed in the table. Ions start on the left side.

### Deceleration

In figure 4.12 the ions have an initial kinetic energy of 23 keV. The particles are created with a random spacial distribution within  $\pm 4$  mm and a random angular distribution within a half angle of  $0.5^\circ$ . The beam profile of a 23 keV  $^{63}\text{Cu}^-$  beam at ILIAS was determined by measurement with the slits between the analyzing magnet and the cooler. At that point the beam diameter was 8 mm, which justifies the assumption on the beam parameters in the simulation.

When passing the aperture, the particles are decelerated to an injection energy of 30 eV. The strong deceleration leads to an angular divergence of the beam of  $45^\circ$ . With the used beam parameters about 10% of the initial ions are lost on the low lens and another 25% on the injection aperture. These losses decrease for a smaller beam size and vanish for an initial beam diameter of 2.5 mm.

### Re-acceleration

The simulation of the re-acceleration was split in two parts. The first simulation (see figure 4.13) intends to provide a realistic assumption on the beam parameters at extraction from the quadrupole. It includes the last 40 mm of the electrode structure, the cooler tube, the aperture and the low lens. The gas is not included in the simulation, but the initial beam parameters are those of an already cooled beam in equilibrium with the gas. The resulting beam was used as input for the simulation of the complete extraction including the cooler aperture, both re-acceleration electrodes and the ground electrode (see figure 4.14).

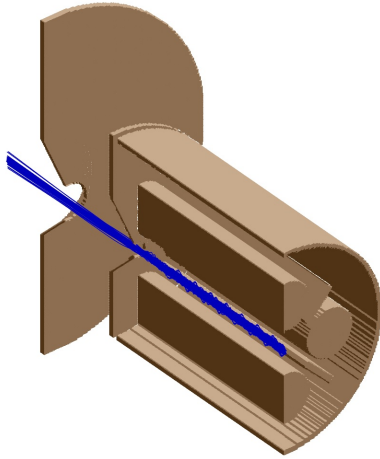


Figure 4.13.: SIMION simulation of extraction with the last 40 mm of the electrode structure, cooler tube, conical cooler aperture and conical extraction low lens.

Settings: initial random ion distribution within circle of 0.8 mm, half angle (filled):  $20^\circ$ , initial energy: 0.1 eV, mass: 63, RF frequency: 2 MHz, RF voltage: 200 V, GELEC:  $-60$  V, low lens: 400 V, cooler tube and aperture on ground.

In the simulation of the whole re-acceleration section (figure 4.14), the particles are created right before the extraction aperture with a half angle of  $30^\circ$  and an initial energy of 7 eV. This corresponds to the energy that cooled ions gain when they traverse the potential difference between the cooler and the aperture, if  $\text{GELEC} = -60$  V. After the acceleration towards the ground electrode the beam shows only little divergence and has a beam diameter of roughly 3 mm.

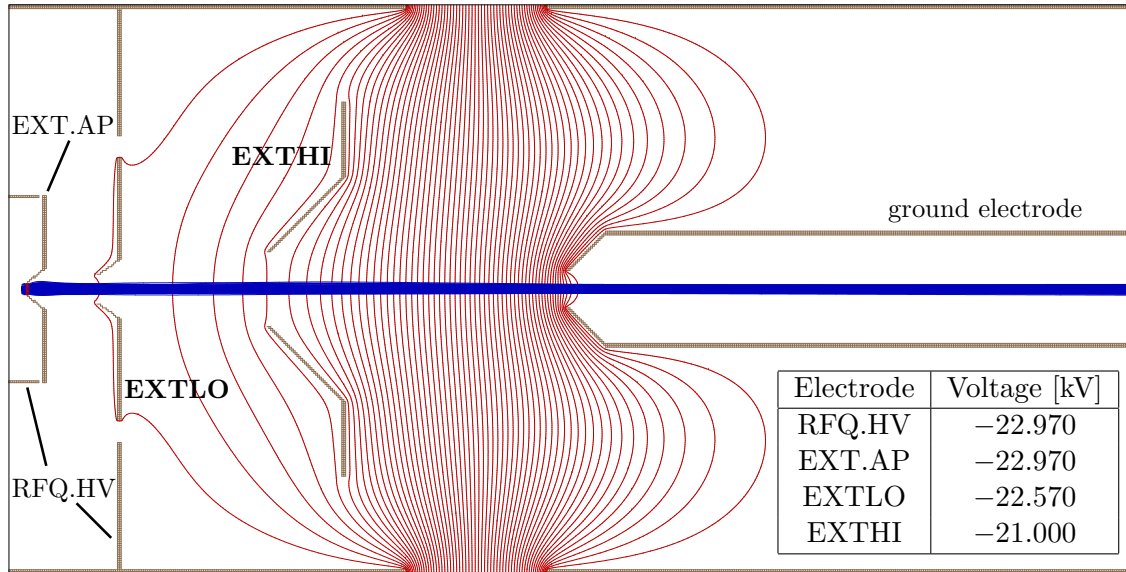


Figure 4.14.: Simulation of the re-acceleration section with equipotential contours (red) and ion trajectories (blue). The voltages on the electrodes relative to lab ground are listed in the table. Ions start on the left side.

## 4.6. Transmission

If not otherwise specified, transmission means the ratio of ion beam current in FC 2 (extracted current) to FC 1 (current after magnet) given in %. In the following paragraphs all major modifications are listed in the correct order along with the transmission of a cooled  $^{63}\text{Cu}^-$  ion beam at each stage.

### Modification I

Guiding electrodes fixed with holders  $\Rightarrow$  guiding electrodes do not steer any more  
 Injection and extraction sleeves  $\Rightarrow$  prevent spacer from charging  
 $\Rightarrow$  diagnostic

**Transmission: 0%**

Despite all efforts no cooled ion beam could be extracted from the cooler. However, it could be measured on the extraction sleeve and photodetachment studies with the cooled ion beam were possible.

### Modification II

QuadSupport at extraction side  
 instead of QuadSupportAperture  $\Rightarrow$  electrodes uncovered in center  
 Conical extraction low lens  $\Rightarrow$  smaller effective cross section  
 Conical extraction aperture  $\Rightarrow$  aperture closer to electrode structure  
 $\Rightarrow$  1 mm pumping gap  
 $\Rightarrow$  diagnostic

**Transmission: 8%**

After these modifications a cooled ion beam could be extracted from the cooler for the first time. Due to a bad contact, the extraction low lens was on a floating potential and

caused a blocking of the beam. The disturbing potential could be unset in several ways by provoking a discharge. At this stage the transmission from FC 2 to FC 5 was so poor that photodetachment experiments with the extracted beam had only limited significance because of the small ion currents.

### Modification III

QuadSupport at injection side

instead of QuadSupportAperture  $\Rightarrow$  electrodes uncovered in center

Conical injection aperture  $\Rightarrow$  aperture closer to electrode structure  
 $\Rightarrow$  diagnostic

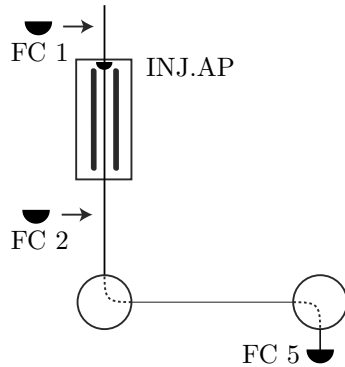
X/Y-steerer after cooler  $\Rightarrow$  improved transmission from FC 2 to FC 5

Pumping holes enlarged  $\Rightarrow$  variable pumping gap 1 – 10 mm

**Transmission: 44%**

The mounting of a new steerer after the cooler improved the transmission into FC 5 drastically. It corrects for any misalignment of the cooler tube and re-acceleration electrodes, which is important for proper injection into the electrostatic beam bender BEN020 (see figure 1.5), that has a 10 mm aperture. Besides these modifications the bad connection of the floating extraction lens was identified and fixed. Unfortunately the cooler had to be reopened two times because the RF connections and some broken pins had to be replaced.

For a 300 nA  $^{63}\text{Cu}^-$  beam of 23 keV, overall transmissions of up to 44% could be achieved after the third modification. The biggest losses happen at the injection. 34% of the beam was measured on the cooler aperture at the injection side. The transport and extraction efficiency of the beam that is captured by the quadrupole field at the cooler entrance is more than 80%. The following ion currents were measured.



Position	Ion Current [nA]
FC 1	293
INJ.AP	100
FC 2	129
FC 5	122

Figure 4.15.: Detailed view of the ILIAS setup.

For this beam the enlarged pumping holes did not improve the transmission. They only raise the gas consumption and lower the pressure in the cooler tube. Cooling times become longer and the residence time in the cooler is reduced, which results in less effective laser photodetachment. For the copper beam it was best to keep the shells closed, where only the 1 mm pumping gap remains.

The losses on the injection aperture can be explained by the wide ion beam. The simulation discussed in the previous section shows that the injection efficiency improves as the beam diameter gets smaller. The ILIAS suffers from very bad ion optical properties on the

injection side caused by the limited lab space available. The quality of the ion beam is expected to increase significantly once the cooler setup along with the new injector are installed properly at the VERA site. Measurements also show that the transport efficiency of the cooler can be further improved by a higher RF voltage, which is impossible with the current RF setup.

## 4.7. Tuning of the Cooler

The ion beam cooler is a complicated system to tune because it has a large number of correlated parameters. This is a summary of our procedure for tuning the cooler from scratch.

- As a first approximation for a straight injection into the cooler, tune the injector to FC 1, then to FC 2 (EEL010, ESX030, ESY040, EEL050, BMH060, MSY070), while all cooler components are still turned off.
- Turn on the cooler high voltage RFQ.HV such that the injection energy is about 100 eV.
- Connect all eight electrodes to a low noise amplifier and tune the injection lenses INJLO and INJHI for maximum current injection into the cooler.
- Reconnect the electrodes as usual and tune RF voltage and amplitude. The reading of FC 2 should at least double.
- Fill in the buffer gas, such that the reading on GIN10 is about 0.1 - 0.2 mbar. (The gas supply line from the bottle to the needle valve has to be pumped and then put under He pressure >1 bar while the HV is still off!)
- Tune the extraction lenses EXTLO and EXTHI and the guiding electrodes GELEC to FC 2.
- Tune all components, including the gas pressure, injector and cooler components, to FC 2. If there is no current in FC 2, lower the cooler HV. Gradually rise the cooler HV, always retuning all components.
- After optimization of the cooler and injector components to FC 2, the extracted beam can be tuned to FC 5. Parameters to tune to FC 5 are the lenses EXTLO and EXTHI, the electrostatic steerer STEERER.X and STEERER.Y and the electrostatic benders BEN020 and BEN010.

Additional notes:

- ◊ The optimum for the injector setup with gas usually differs from the initial tuning without gas, because it has to correct for any misalignment of the injection lenses that shows an effect only when the ions are decelerated.
- ◊ The injection energy of singly charged ions is  $(\text{SIS.CAT} + \text{SIS.HV} - \text{RFQ.HV} - 210 \text{ V})e$ . The offset was determined by measurement of the cooler and source high voltage with a probe. For example, if the source potential is nominally  $-23.000 \text{ keV}$  and the cooler is set to  $-23.196 \text{ keV}$  (like it is in the parameter list below), then the ions have an injection energy of 14 eV.

- ◇ The potentials of the guiding electrodes and the cooler add up. In the above case, a voltage of GELEC=−80 V and more would prevent the beam from entering the quadrupole because the on-axis potential of the guiding electrodes would exceed −14 V relative to cooler high voltage.
- ◇ For fine tuning, the voltages on the power supplies placed in the safety cage have to be changed slowly. The data transfer in and out of the cage has a certain time delay. It takes about one second until equilibrium conditions in the cooler have been established after the voltages on the guiding electrodes and the cooler lenses were changed.
- ◇ Since injection and extraction of the cooled beam can be regarded as independent from each other there should be no need to change any of the injection parameters when tuning the extracted beam.
- ◇ The ILIAS cooler has a maximum in transmission for operation at a Mathieu parameter of about  $q = 0.5$  (see section 5.4).
- ◇ The transmission is roughly constant below 1  $\mu\text{A}$  injected current (FC 1). Above that space charge effects become important and limit the total current that can be transported by the quadrupole.
- ◇ The best setting for the voltage on the guiding electrodes is usually around −15 V (at least for Cu). Even at zero voltage a large part of the beam is transmitted. It seems as if the injected space charge was sufficient to push the ions through the electrode structure.

This list of parameters is the final setup of the measurement with the 23 keV  $^{63}\text{Cu}^-$  beam that was already discussed in the end of the previous section (see figure 4.15).

Component	Control Value
SIS.CAT	−6.000 kV
SIS.HVS	−17.000 kV
EEL010	12.666 kV
ESX030	−14.547 V
ESY040	−49.239 V
EEL050	0.000 kV
BMH060	27.874 A
MSY070	0.198 A
RFQ.HV	−23.196 kV
INJHI	3.206 kV
INJLO	1.053 kV
GELEC	0.000 V
EXTLO	1.172 kV
EXTHI	2.291 kV
DS345.FREQ	2.000 MHz
STEERER.X	498 V
STEERER.Y	−716 V
BEN020	17.276 kV
BEN010	20.000 kV

## 5. Measurements and Results

During the commissioning phase of the cooler carbon and copper were used as test ions. Both, a carbon cathode and a pure copper cathode, provide intense negative ion beams of several  $\mu\text{A}$  with low contamination at mass 12 and 63, respectively. C (EA=1.26 eV) and Cu (EA=1.24 eV) can be easily detached with the available green laser of 532 nm wavelength, corresponding to an energy of 2.33 eV. The first tuning of the cooler was done with  $^{12}\text{C}$  which turned out to have a mass too low to be efficiently captured and transported in the quadrupole with the RF setup available. In order to reach a higher transport efficiency and better capturing of the ions at the injection into the quadrupole, we decided to work with  $^{63}\text{Cu}$  rather than  $^{12}\text{C}$ , where higher RF amplitudes can be obtained at the same Mathieu  $q$  according to equation 2.12. Also, the threshold for collisional detachment lies at a larger injection energy for  $^{63}\text{Cu}$  (20.7 eV) as compared to  $^{12}\text{C}$  (5.0 eV) due to the larger mass.

In the following section selected measurements are discussed that were carried out during the four stages of development of the cooler. For a summary of the modifications made to the cooler system, see section 4.6.

### 5.1. Original Design

Photodetachment studies at ILIAS had already been performed in a crossed beams setup before the cooler was built [14]. During these experiments a magnetic quadrupole triplet was put in its place. After the cooler was built it replaced the quadrupole triplet. The VERDI V18 laser was tuned for collinear ion-laser overlap in the cooler with the transmitted laser power being measured in the power meter after the bending magnet. The original cooler design did not allow the extraction of cooled ion beams, therefore a first demonstration photodetachment experiment with the collinear setup was performed without cooling the ions.

For the experiment a mass 12 ion beam from a carbon cathode was used. The initial beam energy was 16.000 keV, the cooler HV set to  $-15.500$  kV, therefore the injection energy into the quadrupole was 710 eV (taking into account the offset of 210 V between source and cooler HV). The buffer gas pressure measured in the gas inlet line was  $\text{GIN}_{10}=0.030$  mbar, which is not sufficient to stop and cool the ions to equilibrium. With the original design even a small voltage on the guiding electrodes caused a steering effect, therefore they were kept turned off during all experiments presented in this section. The RF was used, which in case of an uncooled beam doubles the ion current after the cooler compared to the situation without RF. The following ion currents were measured in the Faraday cups (see figure 1.5 for sketch of the setup).

FC SIS	16 $\mu$ A
FC 1	3 $\mu$ A
FC 2	1 nA
FC 3	800 pA
FC 4	9 pA
FC 5	5 pA

With the original design, the transmission through the cooler system and the transport efficiency after the cooler were so low that the beam in the offside cups (FC 4 and FC 5) was close to the detection limit of 1 pA. Figure 5.1 shows the ion current in FC 4 (black) while turning off and on the laser. The transmitted laser power was 10 W. The logical signal (green) represents the states laser off (low) and laser on (high). When the laser was turned on, the current dropped by 8%.

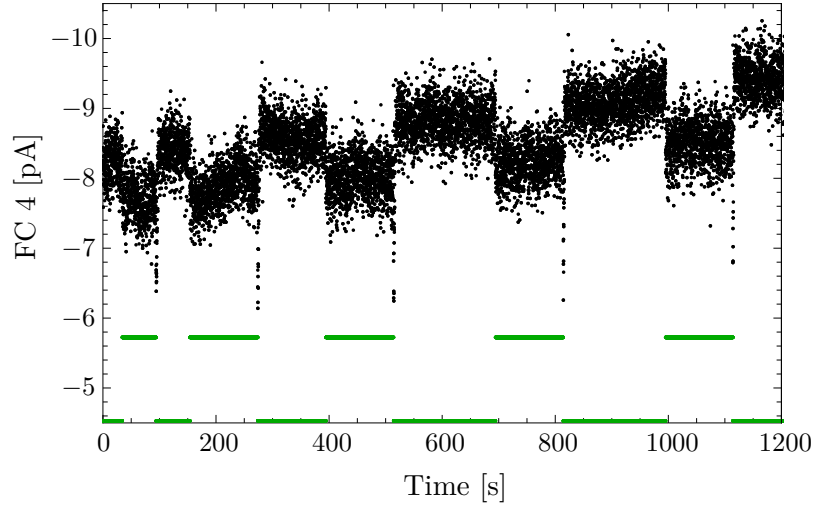


Figure 5.1.:  $^{12}\text{C}^-$  beam of 16.0 keV measured in FC 4. The logical signal (green) represents the states laser off (low) and laser on (high). The transmitted laser power of 10.0 W was measured in the power meter after the analyzing magnet.

The measured suppression can roughly be reproduced with the following estimation. The ions have an energy of 710 eV, corresponding to a residence time of 7.5  $\mu$ s in the cooler. The laser power inside the cooler is expected to be about 12 W, which is 20% higher than the power transmitted to the power meter after the analyzing magnet, due to losses on the cooler aperture and the exit window. Assuming that the 12 W of a 532 nm laser are uniformly distributed over a disc of 3 mm diameter gives a photon flux of  $4.6 \times 10^{20} \text{ cm}^{-2}\text{s}^{-1}$ . The cross section for laser photodetachment of  $^{12}\text{C}^-$  at 532 nm wavelength is  $1.4 \times 10^{-17} \text{ cm}^2$  [41]. Inserting the ion-laser interaction time  $t$ , the photon flux  $\phi$  and the cross section for photodetachment  $\sigma$  into  $D(t) = 1 - e^{-\phi\sigma t}$  gives a depletion of 5%, which is close to the measured value, considering the rough assumptions in the beginning of the calculation.

Figure 5.2 shows scans of the cooler HV without a buffer gas and with 0.03 mbar He

buffer gas. The  $^{12}\text{C}$  ion current was measured in FC 2, the cup right after the cooler. The initial ion energy was 16.0 keV. Without gas (figure 5.2a) the negative ion beam passes the cooler and decreases in intensity as the cooler HV is raised. Raising the cooler HV means that the injection energy is lowered, resulting in a larger angular divergence of the beam and bigger losses at the injection. A local maximum in transmission appears for RFQ.HV=15.9 kV (310 eV injection energy), because the cooler parameters were optimized for that value. The other highly developed maxima always appear when transporting an uncooled beam in the quadrupole. Their position and relative intensities depend on the tuning of the cooler parameters. It has to be mentioned that the lenses were turned on during the scan of the high voltage, stating small deceleration sections for the fast ions at small cooler HV.

At a He buffer gas pressure of 0.03 mbar (figure 5.2b) a positively charged ion beam is transmitted to FC 2 for a cooler HV up to 8 kV which is half-way between the initial ion energy and lab ground. If the injection energy is further decreased, a negatively charged beam is detected in FC 2. This phenomenon can be explained through charge changing processes in the gas. When the negative ion beam traverses the gas-filled region, the ions undergo charge changing processes through collisions with the buffer gas atoms. A certain charge state distribution of negative, neutral and positive ions is established. The neutral atoms and multiply positively charged ions cannot be transported in the quadrupole, while the singly charged ions are transported equally, regardless of the sign of the charge. Therefore all  $^{12}\text{C}^-$  and  $^{12}\text{C}^+$  ions can be transmitted to FC 2. Unfortunately it is not possible to determine the exact charge state distribution, however, the positive ions dominate and an overall positive current is observed for cooler voltages below 8 kV. The ions that get singly positively charged inside a cooler potential above 8 kV are trapped inside the cooler and cannot leave towards the beamline on lab ground. Therefore a negative current is detected in FC 2 for injection energies below half of the initial ion energy.

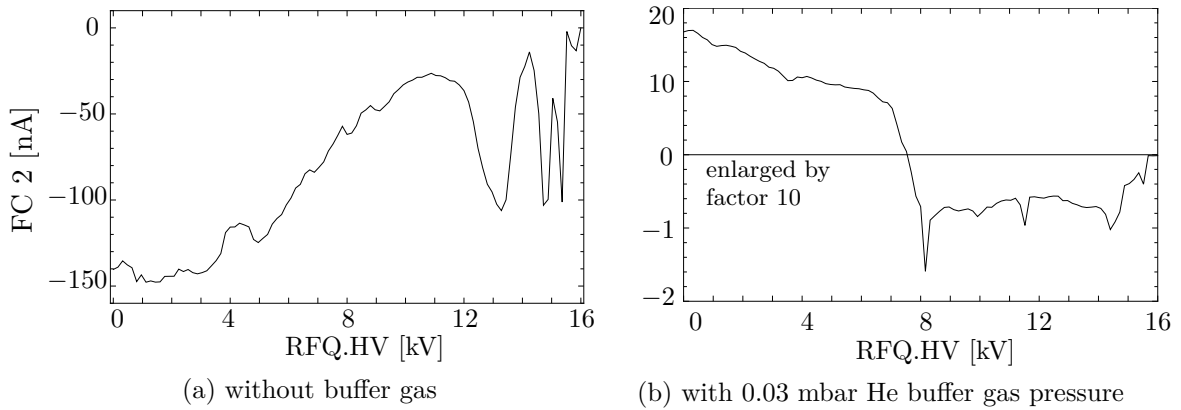


Figure 5.2.:  $^{12}\text{C}$  current measured in FC 2 as function of cooler HV. The initial ion energy was 16.0 keV. With buffer gas, a certain fraction of the ions is stripped to the  $1+$  charge state and a positive ion current can be extracted from the cooler. In (b) the scale for negative values is enlarged by a factor of 10.

## 5.2. Modification I

With the original design it was not possible to extract a cooled ion beam. Due to the lack of diagnostics tools it was also impossible to find out where the ion losses happened. After the first modification the cooled beam could still not be extracted, however, the extraction sleeve provided an important diagnostics tool inside the cooler that enabled the first photodetachment study of a cooled ion beam in the ILIAS cooler. This way the successful cooling and transport of the ions in the quadrupole could be demonstrated.

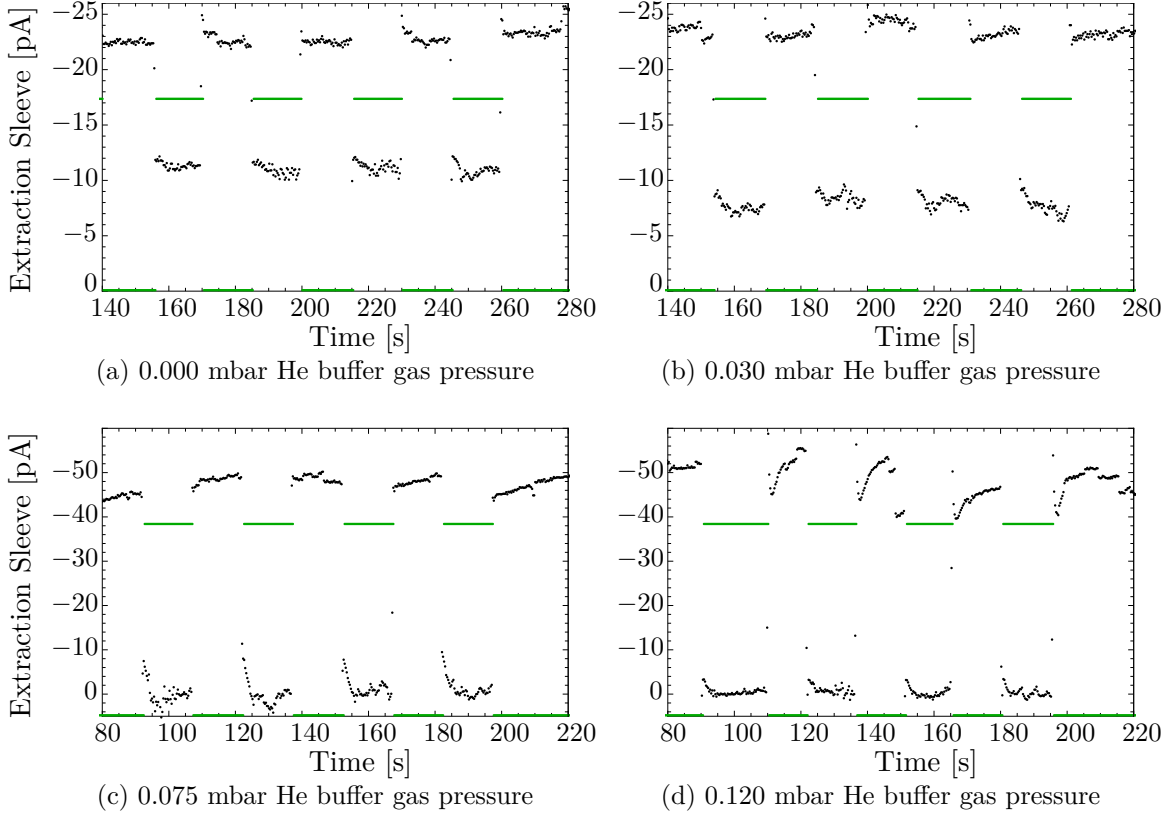


Figure 5.3.:  $^{63}\text{Cu}^-$  ion current measured on the extraction sleeve (black) with laser on and off at different buffer gas pressures. The logical signal (green) represents the states laser off (low) and laser on (high). The transmitted laser power of 10.3 W was measured in the power meter after the bending magnet. The QuadSupportAperture which held the extraction sleeve was made from Teflon. The properties of the material caused an offset in the measurement of the ion current on the metal sleeve of about 80 nA. In each measurement, the baseline was recorded before and after the use of the laser and subtracted from the dataset. The plots show only these corrected data. Later the Teflon spacer was removed. At higher buffer gas pressures, the ions have a longer residence time in the cooler resulting in stronger depletion by photodetachment.

Figure 5.3 shows photodetachment experiments with a  $^{63}\text{Cu}^-$  ion beam at different buffer gas pressures. The ion current was measured on the extraction sleeve. Similar to the measurement presented in the previous section, the green signal represents the states laser on and off. With rising buffer gas pressure the ion-laser interaction time is extended and the fraction of detached ions increases, thus the transmitted current is reduced. Above

0.075 mbar the remaining ion current is below the detection limit.

The cooler was tuned for an injection energy of 160 eV. The short-term fluctuations of the ion current can be explained by source instabilities and the floating potential in the extraction region (EXTLO) at that time. Even though the beam could not be extracted, the experiment demonstrates the benefits of buffer gas cooling. Obviously a sufficiently high buffer gas pressure leads to a higher efficiency of laser photodetachment due to the longer residence time in the interaction region and to an improved capturing and transport of the ions, which becomes apparent in an increased net current on the extraction sleeve.

### 5.3. Modification II

After the second modification the extraction of a cooled ion current was possible under certain circumstances. The transmission to the offside cups (FC 4 and FC 5) was still poor, but sufficient for measurements with FC 4.

The photodetachment experiment at varying gas pressure was repeated, now measuring the ion current in FC 4 instead of measuring on the extraction sleeve. Figure 5.4 summarizes the series of measurements. It gives the  $^{63}\text{Cu}^-$  suppression factor as function of buffer gas pressure. The suppression factor is the ratio between the ion beam currents measured in the offside cup with the laser turned off and on. In most cases the error bars calculated from the scattering of the data is smaller than the point size. Figure 5.5 shows selected plots for a buffer gas pressure of 0.13 mbar, 0.16 mbar and 0.19 mbar. The increasing gas pressure results in an extended ion-laser interaction time  $t$  and the suppression follows the exponential law  $\propto e^{\sigma\phi t}$  (see formula 4.1) as expected.

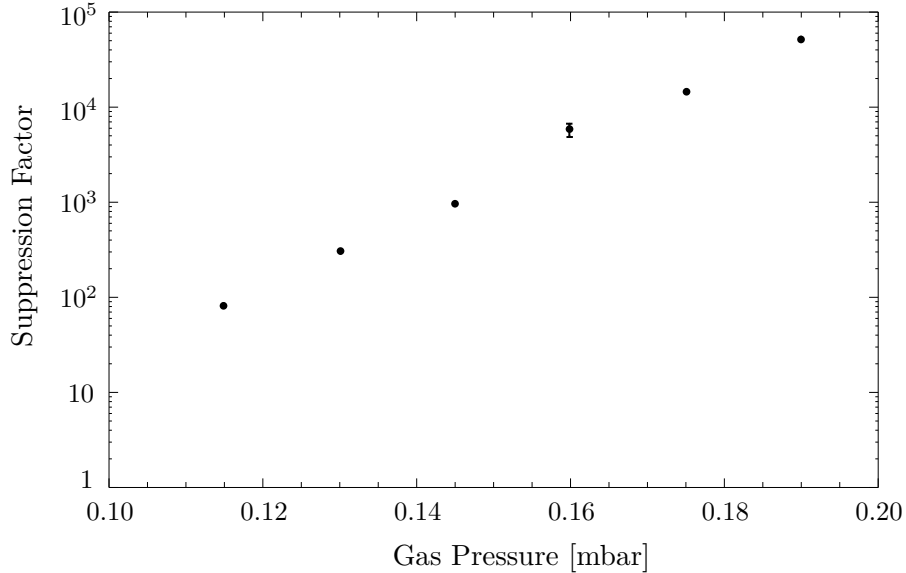


Figure 5.4.: Suppression factor for  $^{63}\text{Cu}^-$  as function of buffer gas pressure measured in vacuum gauge GIN10 with a transmitted laser power of 10 W. The suppression factor is the ratio between the ion beam currents measured in FC 4 with the laser turned off and on, respectively. At higher buffer gas pressures, the ions have a longer residence time in the cooler resulting in stronger depletion by photodetachment.

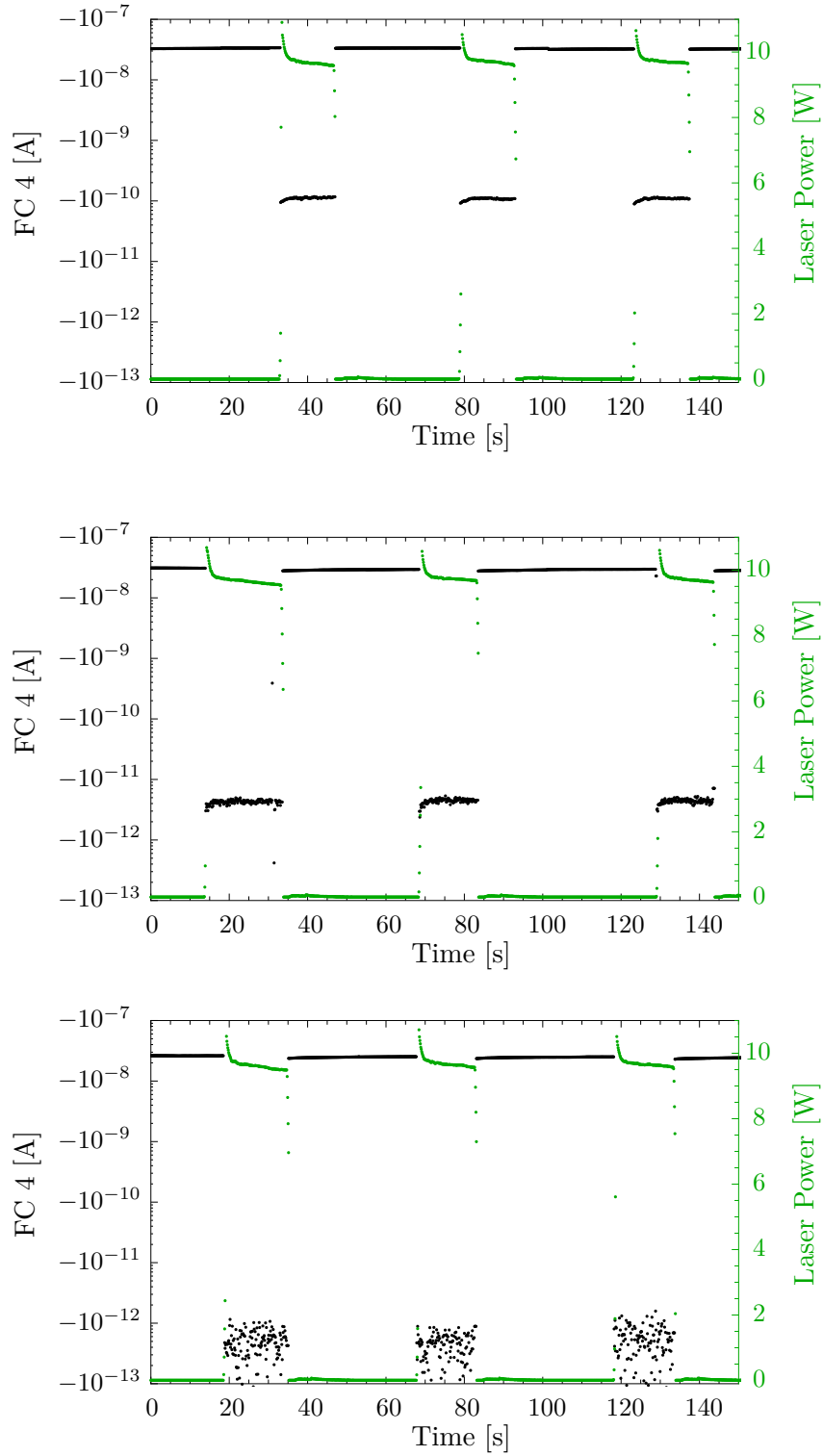


Figure 5.5.:  $^{63}\text{Cu}^-$  ion current measured in FC 4 (black) with laser on and off at different buffer gas pressures measured in vacuum gauge GIN10: 0.130 mbar (top), 0.160 mbar (middle) and 0.190 mbar (bottom). The transmitted laser power was measured in the power meter behind the analyzing magnet (green). The higher initial laser power is caused by the use of the internal shutter of the laser system. The slight drift in the laser curve is an artefact caused by a temperature effect of the power meter.

A second measurement demonstrates the suppression by laser photodetachment as a function of laser power (figure 5.6). The laser power was measured in the power meter behind the analyzing magnet, the ion current in FC 4. Up to a laser power of 6 W the suppression shows the expected exponential behavior, as the laser power is proportional to the photon flux  $\phi$ . The value at 10 W laser power does not fit the curve. Although only one data point deviates from the expected behavior, this measurement already indicates a beam contamination. The behavior was later verified with an ion beam of higher intensity and more data points, as discussed in section 5.4. Figure 5.7 shows selected plots for a laser power of 1 W, 4 W and 10 W.

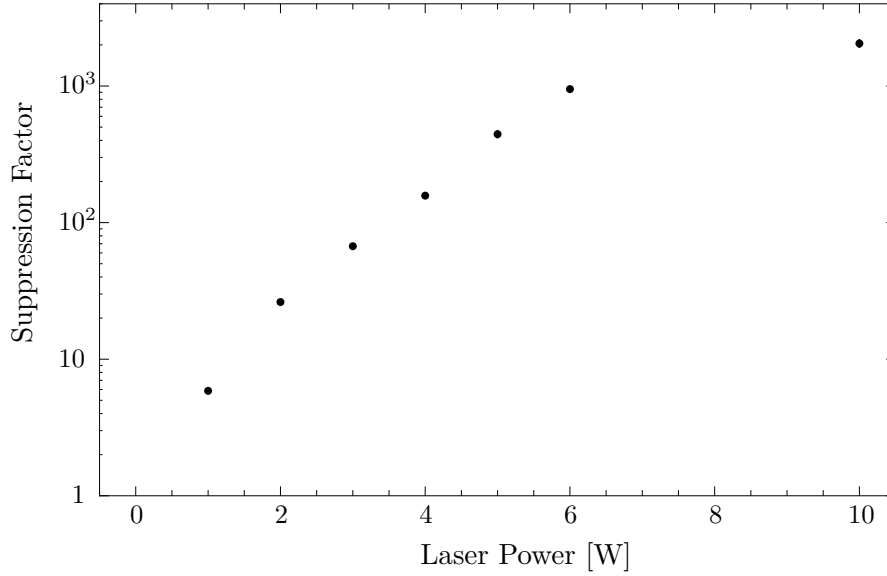


Figure 5.6.: Suppression factor for  $^{63}\text{Cu}^-$  as function of laser power measured in the power meter behind the analyzing magnet at a He buffer gas pressure of 0.124 mbar. The suppression factor is the ratio between the ion beam currents measured in FC 4 with the laser turned off and on, respectively.

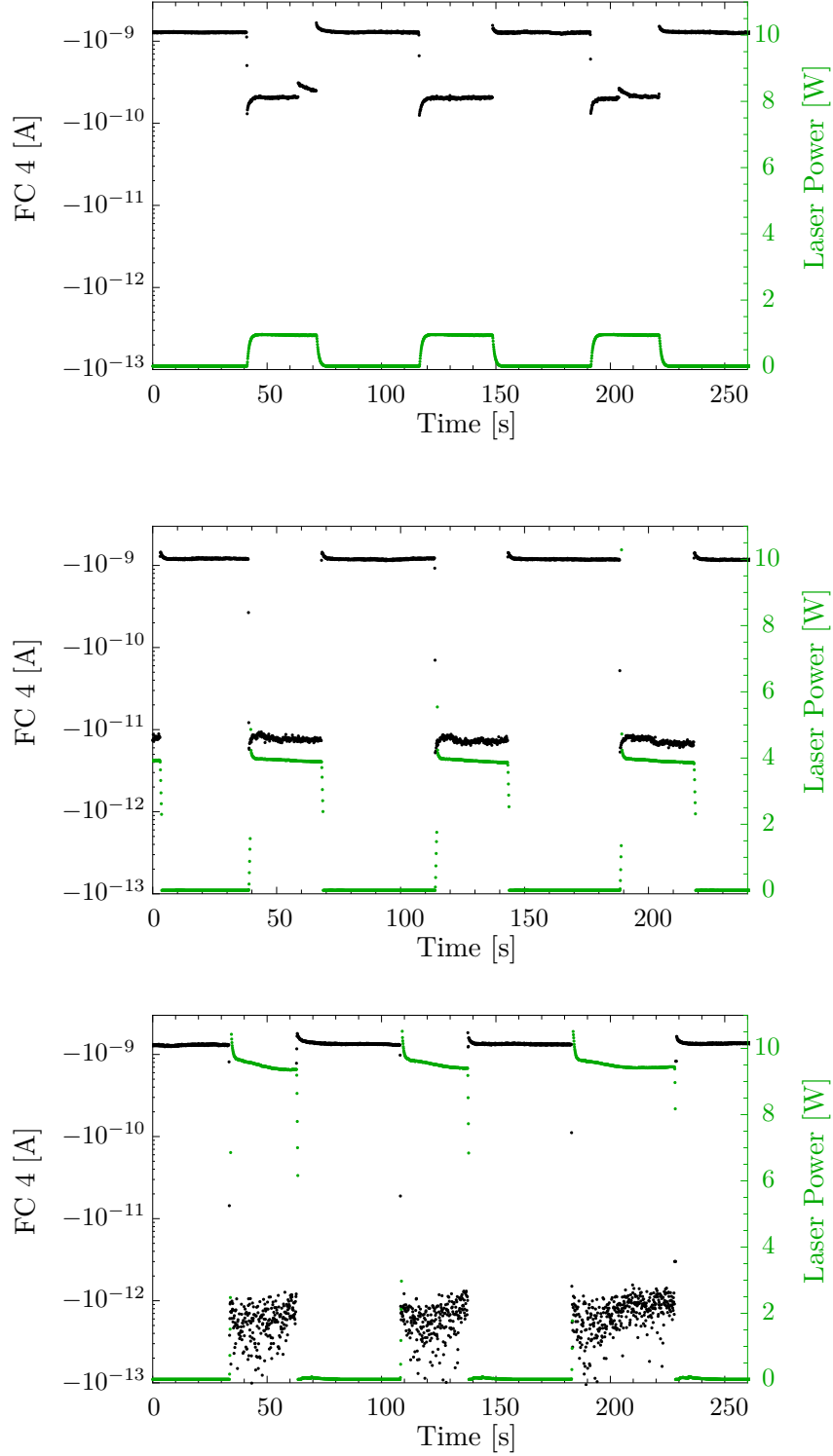


Figure 5.7.:  $^{63}\text{Cu}^-$  ion current measured in FC 4 (black) at a buffer gas pressure of 0.124 mbar measured in vacuum gauge GIN10 for different nominal laser powers: 1 W (top), 4 W (middle) and 10 W (bottom). The transmitted laser power was measured in the power meter behind the analyzing magnet (green). The higher initial laser power is caused by the use of the internal shutter of the laser system. The drift in the laser curve is an artefact caused by a temperature effect of the power meter.

## 5.4. Modification III

The third modification of the cooler finally allowed a permanently undisturbed extraction of the cooled ion beam as well as a transport to the offside cups with only minor losses. With this configuration measurements with a  $^{63}\text{Cu}^-$  ion beam were done that demonstrate the proper functioning of the ion beam cooler and characterize it.

Figure 5.8 shows the  $^{63}\text{Cu}^-$  ion beam current transmitted to FC 2 and to the extraction aperture as a function of He buffer gas pressure. The slidable shells were opened at the injection side (large pumping holes) and closed on the extraction side (1 mm pumping gap between aperture and cooler tube). Due to the larger opening higher buffer gas pressures at the gas inlet were necessary to achieve the same cooling effect as before. The diameter of the uncooled beam is larger than the opening of the extraction aperture (3mm) and up to 35% of the ions are lost on the aperture without buffer gas. As the gas pressure is raised, the cooling of the ions gets more effective and the ions are confined closer to the axis. At about 0.13 mbar He buffer gas pressure the beam transmitted to the Faraday cup has a maximum. The beam diameter is smaller than the aperture and the beam can be extracted without noticeable losses on the aperture. For buffer gas pressures above 0.13 mbar the transmission decreases slightly due to collisional losses (scattering) and space charge effects. For the application of isobar separation, a buffer gas pressure above the point of maximum transmission will be chosen in favor of a longer residence time of the ions in the cooler. The position of maximum transmission in terms of gas pressure differs according to the mass and injection energy of the ion. Heavier masses and higher injection energies require a higher gas pressure for fully cooling the beam.

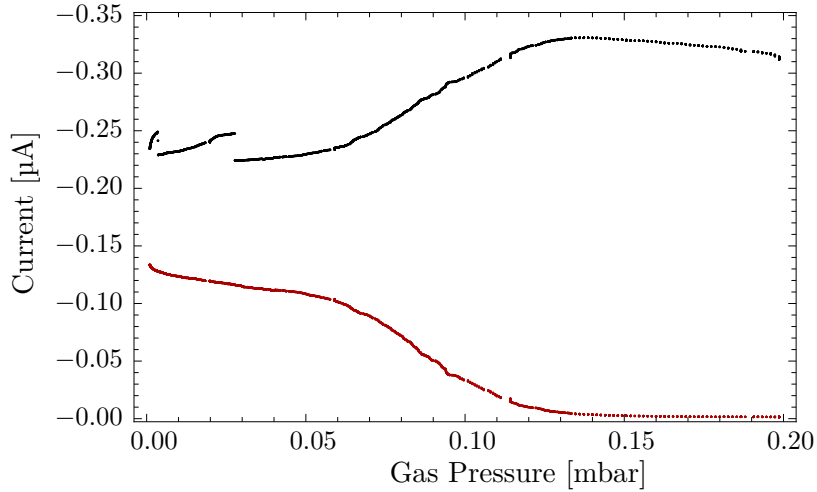


Figure 5.8.:  $^{63}\text{Cu}^-$  ion current transmitted to FC 2 (black) and to the extraction aperture (red) as function of He buffer gas pressure. As the buffer gas pressure rises, the cooling gets more effective. The ions get closer confined to the axis and the losses on the aperture vanish.

The transmission of the ion beam to FC 2 was measured as a function of the Mathieu parameter  $q$  (figure 5.9) for  $\text{Cu}^-$ ,  $\text{AlO}^-$  and  $\text{Cl}^-$ . Thereby the RF amplitude was kept constant at 100 V and the RF frequency was scanned. This is important for a meaningful

measurement since the capturing efficiency at the injection into the quadrupole and the transport efficiency both depend on the absolute value of the RF voltage. The maximum transmission is achieved at  $q=0.55$  for  $^{63}\text{Cu}^-$ ,  $q=0.5$  for  $^{27}\text{Al}^{16}\text{O}^-$  and  $q=0.45$  for  $^{35}\text{Cl}^-$ , which is very well in accord with the results from Iffländer et al [31] shown in figure 2.4.

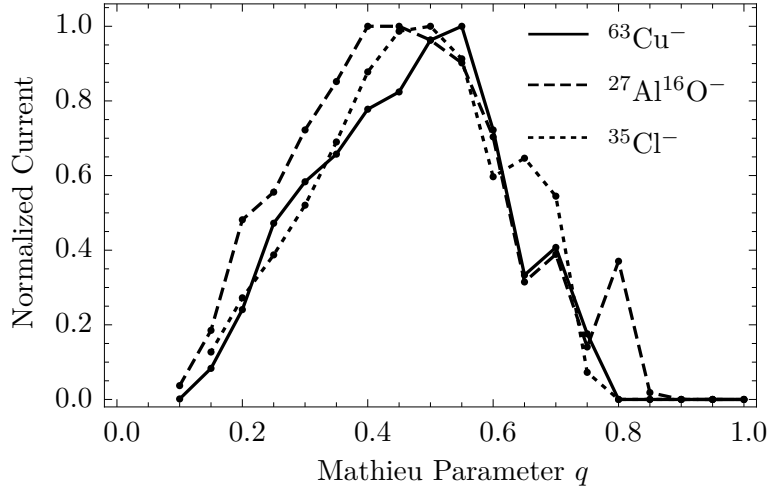


Figure 5.9.: Normalized ion current in FC 2 as a function of the Mathieu parameter  $q$ .  $^{63}\text{Cu}^-$  (solid),  $^{27}\text{Al}^{16}\text{O}^-$  (dashed) and  $^{35}\text{Cl}^-$  (dotted).

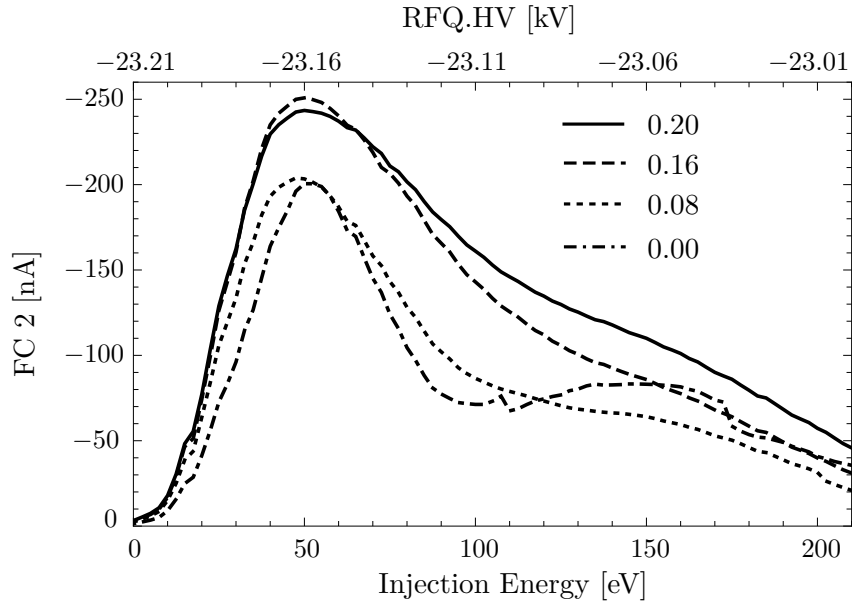


Figure 5.10.:  $^{63}\text{Cu}^-$  current measured in FC 2 as function of injection energy. Regardless of the buffer gas pressure, the optimal injection energy for  $^{63}\text{Cu}^-$  into the cooler is 50 eV (RFQ.HV = -23.16 kV).

The cooler HV is an important tuning parameter since it determines the injection energy of the ions. The optimal injection energy is a compromise between collisional losses towards higher injection energies and losses due to the increasing angular divergence of the

beam towards lower injection energies. Figure 5.10 shows a scan of the cooler HV between  $-23.000$  kV and  $-23.250$  kV for different gas pressures. The source was on a nominal potential of  $-23.000$  kV, corresponding to an initial ion energy of  $23.210$  keV when taking the measured offset into account. Regardless of the buffer gas pressure, the optimal injection energy for  $^{63}\text{Cu}^-$  into the cooler is  $50$  eV (RFQ.HV= $-23.160$  kV) which is above threshold for collisional detachment ( $20.7$  eV). At the optimum injection energy the total losses, which are the sum of collisional losses and losses due to angular divergence, is minimized.

The measurement of the suppression as function of laser power was repeated after the third modification (figure 5.11). For this experiment the slidable shells were closed on both cooler ends, so there was only a  $1$  mm pumping gap between the apertures and the cooler tube. The ion current was measured in FC 5. Figure 5.12 shows selected plots for a laser power of  $0.5$  W,  $1$  W and  $10$  W.

Overall a suppression of the mass 63 beam by almost five orders of magnitude was possible. It is obvious that the suppression factor does not fit the simple exponential law. There are two components, which can be explained by a contamination at mass 63. The contamination has to have a smaller cross section for laser photodetachment at  $532$  nm wavelength as copper, resulting in a twofold exponential behavior  $\propto e^{\sigma\phi t} + e^{\sigma'\phi t}$ . Unfortunately with the available methods at ILIAS it is impossible to distinguish copper from any contamination with non-zero detachment cross section in the remaining beam after the cooler. Once the ion beam cooler is connected to the AMS facility, this behavior can be further analyzed. Therefore the stated suppression factors so far only represent lower limits for the actual suppression of  $^{63}\text{Cu}^-$ .

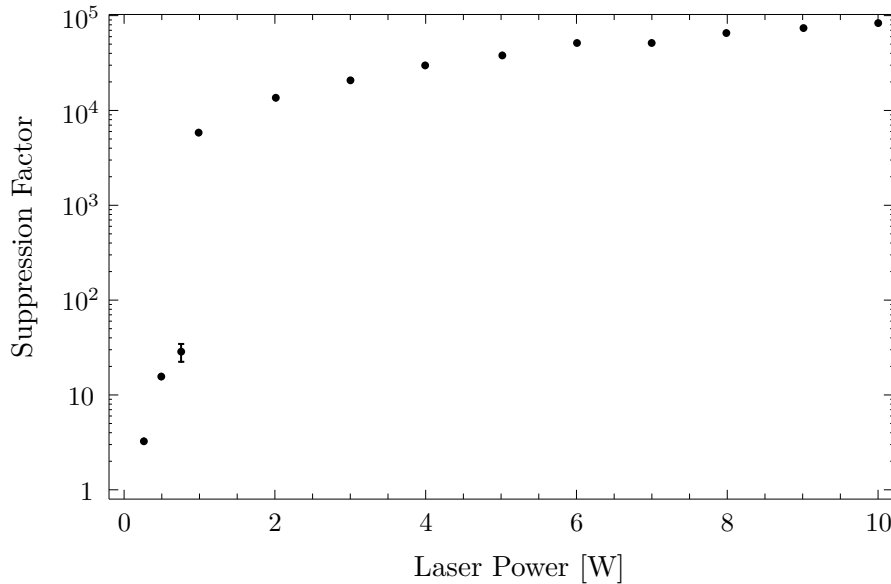


Figure 5.11.: Suppression factor for  $^{63}\text{Cu}^-$  as function of laser power measured with the power meter behind the analyzing magnet at a He buffer gas pressure of  $0.170$  mbar. The suppression factor is the ratio between the ion beam currents measured in FC 5 with the laser turned off and on, respectively. Without the laser the transmitted current was  $70$  nA.

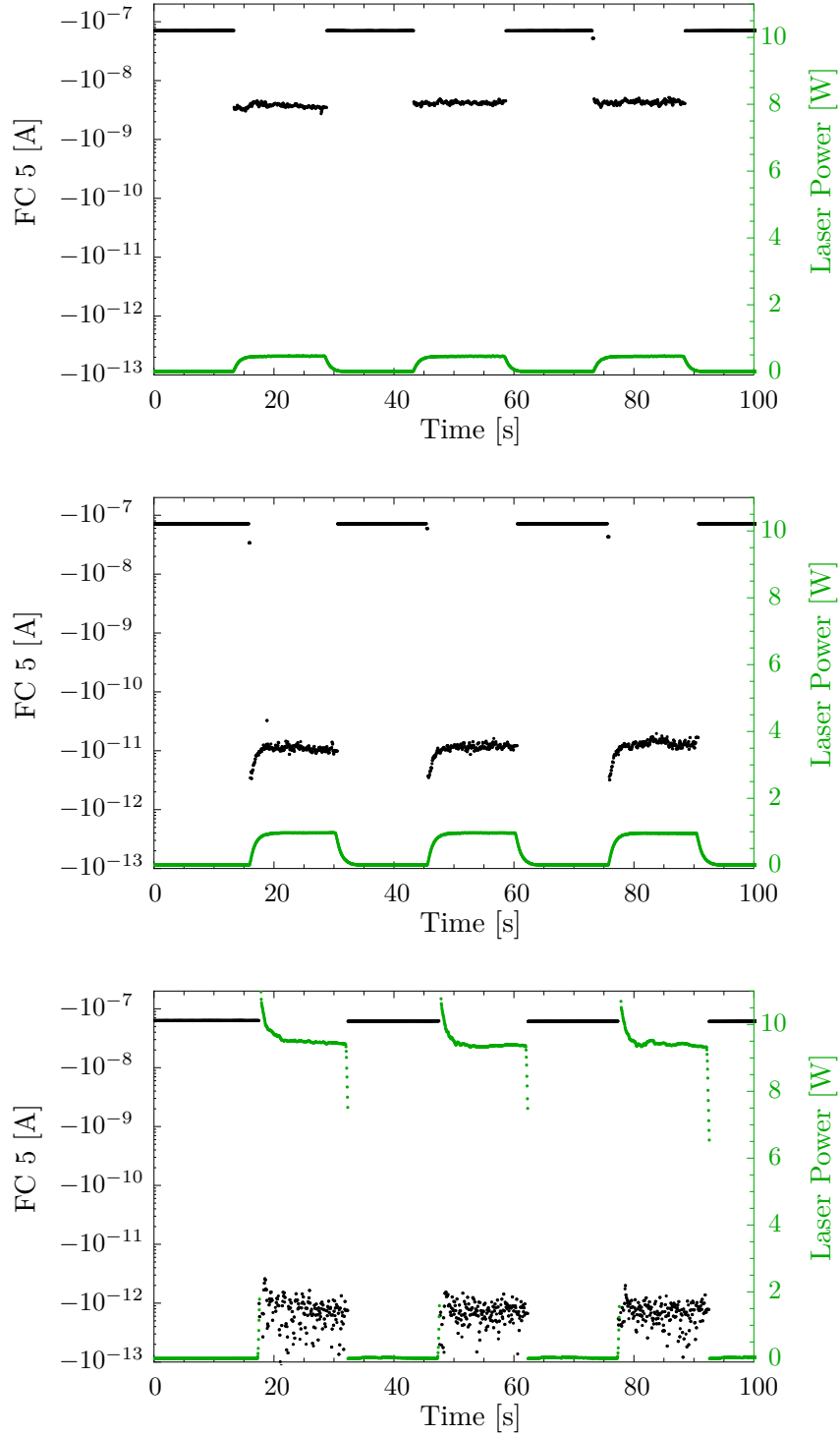


Figure 5.12.:  $^{63}\text{Cu}^-$  ion current measured in FC 5 (black) at a buffer gas pressure of 0.170 mbar measured in vacuum gauge GIN10 for different laser powers: 0.5 W (top), 1 W (middle) and 10 W (bottom). The transmitted laser power was measured in the power meter behind the analyzing magnet (green). The higher initial laser power is caused by the use of the internal shutter of the laser system. The drift in the laser curve is an artefact caused by a temperature effect of the power meter.

## 6. Summary and Outlook

The aim of this Master's project was the commissioning and further development of an ion beam cooler for negatively charged atomic and molecular ions. The feasibility of selective laser photodetachment of the ions in the cooler as a tool for isobar suppression in AMS was demonstrated.

At the beginning of this work, the ion beam cooler was already assembled in its original design but had never been put into operation. After completion of the setup, including the installation of the RF-setup, assembly of beamline parts, the integration of all components into the control system and the implementation of safety measures for the high voltage, the work on the ion beam cooler started. In the beginning the cooling and extraction of the beam was not possible due to almost total beam losses. SIMION simulations provided a better understanding of the cooling process and of the ion optical properties of the device. The stepwise redesign of cooler parts according to those simulations resulted in a steady increase in transmission. After three big modification phases, the ion beam cooler finally worked as expected.

With our test ion  $^{63}\text{Cu}^-$ , the cooler was characterized and we could demonstrate an overall transmission of the device of 44%. The transport and extraction efficiency is in fact more than 80% and we are very optimistic that the losses on the injection side can be further reduced significantly. Ongoing tests with a new RF setup based on a resonant circuit promise higher RF amplitudes which will improve the capturing and transport efficiency of the cooler and will allow the efficient transport of higher currents at least in the low  $\mu\text{A}$  range. In first photodetachment experiments a suppression of the mass 63 beam by almost five orders of magnitude was achieved. The ongoing experiments with  $\text{AlO}$  and  $\text{MgO}$  as well as  $\text{Cl}$  and  $\text{S}$  are very promising and already provide a proof of principle for optical filtering of negative ion beams in an ion beam cooler.

The test bench is limited in space and detection methods and suffers from ion optical deficiencies. The single cathode sputter source is rather stubborn and the availability of an ion beam of appropriate quality is not guaranteed. These difficulties will soon be overcome once the cooler setup is moved in its final place. The accelerator lab has already been extended and the ion beam cooler can be connected to VERA as soon as the analyzing magnet and the electrostatic analyzer are available. The ion source is already there. It has a target wheel that holds up to 134 samples to be compared to the single cathode source that we have at ILIAS now. The new injector will provide beams of higher quality. An xy-steerer right before the cooler entrance and a redesign of the injection aperture will also help improve the transmission significantly.

Once the cooler setup is connected to VERA, first experiments with isobaric systems can be performed. The first test case will be the suppression of  $\text{MgO}^-$  versus  $\text{AlO}^-$ , the oxide of the rare radionuclide  $^{26}\text{Al}$ . The atomic isobars can already be separated in the multi-anode ionization chamber which makes it the perfect isobaric system for demonstrating the efficiency of laser photodetachment in the ion beam cooler. However, the

final goal of the project is to measure isotopic ratios of other rare, long-lived radionuclides currently inaccessible to AMS. One very interesting case to be studied is the ratio  $^{182}\text{Hf}/\text{Hf}$ . The use of laser photodetachment for suppression of the background from stable  $^{182}\text{W}$  is going to push the detection limit further down which might reveal a signal from supernova-produced  $^{182}\text{Hf}$  on earth.

Besides the extension of the range of radionuclides accessible to AMS, also excited states in molecular ions and the possibility of cooling them with buffer gas are going to be under investigation. The integration of ILIAS into the AMS facility will turn VERA into the world's first LAMS (laser-assisted AMS) facility and will open up opportunities never seen before.

## A. SIMION Simulation of Buffer Gas Cooling

SIMION supports different kinds of geometry input and user programming. Import from CAD files is possible, but the current version SIMION 8.1.1 does not support all geometry features with CAD import. When using the new 'surface enhancement' feature, input from a .gem file is necessary. This feature, new in SIMION 8.1, can do fractional grid units, which is crucial for simulating the effect of the tilted guiding electrodes.

A convenient way of user programming is via a .lua file. When installing SIMION, a Lua compiler is automatically included. There are several SIMION-specific function segments and variables that can be used within such a Lua program. In the following the geometry file (.gem) and the user programs (.lua) used for the buffer gas simulation are given.

### A.1. Geometry

```
;cooler.gem creates the geometry for the electrode structure
;Author: Johanna Pitters

;electrode 1 : opposite RF electrodes
;electrode 2 : opposite RF electrodes
;electrode 3 : tilted guiding electrodes
;electrode 4 : cooler tube
;scaling : 0.25mm/gu

pa_define(85,85,3200,planar,xy_mirror,Elect,surface=fractional)
e(1){
    ;electrode 1 RF
    fill{within{cylinder(38,0,3200,20,,3201)}}
}
}

e(2){
    ;electrode 2 RF
    fill{within{cylinder(0,38,3200,20,,3201)}}
}
}

e(3){
    ;electrode 3 guiding electrodes
    locate(0,0,0,1,0,-45,0){
    locate(0,0,0,1,0,0,-0.035){
        fill{within{box3d(-3,26,-10,3,55,3210)}}
        within{cylinder(0,25,3200,3,,3201)}}
    }
}}
```

```
}
e(4){                ;electrode 4 cooler tube
    fill{within{cylinder(0,0,3200,84,,3200)}
        notin{cylinder(0,0,3200,80,,3201)}
    }
}
```

### A.2. Viscous Damping Model

```
-- SIMION 8.1
-- Quadrupole with tilted guiding electrodes
-- Ion motion is damped by linear damping term
-- Author: Johanna Pitters

simion.workbench_program()

os.remove("results_damp.csv")
local results_file = assert(io.open("results_damp.csv", "w"))
results_file:write("ToF velocity Ekin Distance py pz \n")

adjustable d = 0          -- linear damping time constant (1/usec)
adjustable rf_frequency = 2.5 -- frequency (1/usec)
adjustable rf_amplitude = 200 -- RF amplitude
adjustable gelec = -50.0   -- voltage on guiding electrode (V)

--SIMION initialize segment. Randomizes particle's time of birth.
function segment.initialize()
    ion_time_of_birth = rand() / rf_frequency
end

--SIMION init_p_values segment. Sets constant voltages.
function segment.init_p_values()
    adj_elect03 = gelec
    adj_elect04 = 0
end

-- SIMION fast_adjust segment. Sets RF electrode potentials.
function segment.fast_adjust()
    adj_elect01 = rf_amplitude * sin(ion_time_of_flight *
        2 * math.pi * rf_frequency)
    adj_elect02 = -adj_elect01
end

-- SIMION accel_adjust segment. Adds damping term to ion's acceleration.
function segment.accel_adjust()
    if ion_time_step == 0 then return end -- skip if zero time step
    if d == 0 then return end             -- skip if damping is zero
```

```

    ion_ax_mm = (ion_ax_mm - d * ion_vx_mm)
    ion_ay_mm = (ion_ay_mm - d * ion_vy_mm)
    ion_az_mm = (ion_az_mm - d * ion_vz_mm)
end

-- SIMION other_actions segment. Saves data to file.
function segment.other_actions()
    -- Compute ion velocity
    local speed_ion = sqrt(ion_vx_mm^2 + ion_vy_mm^2 + ion_vz_mm^2)

    -- Compute ion kinetic energy
    local kenergy_ion_eV = (speed_ion^2) * 0.0051722 * ion_mass

    -- Compute ion distance from center
    local distance_ion_mm = sqrt(ion_px_mm^2 + ion_py_mm^2)

    results_file:write(ion_time_of_flight.." "..speed_ion.." "
        ..kenergy_ion_eV.." "..distance_ion_mm.." "
        ..ion_py_mm.." "..ion_pz_mm.."\\n")
    results_file:flush()
end

function segment.terminate()
    results_file:close()
end

```

### A.3. Hard-Sphere Model

```

-- SIMION 8.1
-- Quadrupole with tilted Guiding Electrodes
-- Author: Johanna Pitters
-- Collisional cooling based on
--   collision_hs1.lua
--   A hard-sphere, elastic, ion-neutral collision model for SIMION 8.
--   REVISION-4-2007-02
--   http://www.simion.com/issue/362
--   Author David Manura, 2005-06
--   (c) 2006 Scientific Instrument Services, Inc. (Licensed under SIMION 8.0)

simion.workbench_program()

---- Global variables
adjustable _rf_frequency = 2.6          -- frequency (1/usec)
adjustable _rf_amplitude = 200         -- RF amplitude (V)
adjustable _gelec = -50.0              -- voltage on guiding electrodes (V)
adjustable _gas_mass_amu = 4.0         -- Mass of buffer gas particle (amu)
adjustable _temperature_k = 300.0      -- Buffer gas temperature (K)

```

## CHAPTER A. SIMION Simulation of Buffer Gas Cooling

---

```
adjustable _pressure_pa = 1      -- Buffer gas pressure (Pa)
adjustable _sigma_m2 = 3.14e-19 -- geometric cross section (m^2)
                                -- default for He and Cl-
adjustable _steps_per_MFP = 20.0 -- Mean number of time steps per MFP.
adjustable _mark_collisions = 1  -- If non-zero, collisions will be marked.

---- Internal variables
local last_ion_number = -1
local last_speed_ion = -1
local k = 1.3806505e-23      -- Boltzmann constant (J/K)
local kg_amu = 1.6605402e-27 -- (kg/amu) conversion factor
local eV_J = 6.2415095e+18   -- (eV/J) conversion factor

local mean_free_path_mm = -1
local max_timestep      -- Updated so that _steps_per_MFP is meaningful
local v_eff = -1

os.remove("results_coll.txt")
local results_file = assert(io.open("results_coll.txt", "w"))
results_file:write("ToF MFP velocity Ekin Distance py pz\n")

function gaussian_random()      -- Using the Box-Muller algorithm.
    local s = 1
    local v1, v2
    while s >= 1 do
        v1 = 2*rand() - 1
        v2 = 2*rand() - 1
        s = v1*v1 + v2*v2
    end
    local rand1 = v1*sqrt(-2*ln(s) / s)
    return rand1
end

-- SIMION initialize segment. Randomizes particle's time of birth.
function segment.initialize()
    ion_time_of_birth = rand() / _rf_frequency
end

-- SIMION init_p_values segment. Sets constant voltages.
function segment.init_p_values()
    adj_elect03 = _gelec
    adj_elect04 = 0
end

-- SIMION time step adjust segment.
-- Ensures time steps are sufficiently small.
function segment.tstep_adjust()
```

```

    if max_timestep and ion_time_step > max_timestep then
        ion_time_step = max_timestep
    end
end

-- SIMION fast_adjust segment. Sets RF potentials.
function segment.fast_adjust()
    adj_elect01 = _rf_amplitude * sin(ion_time_of_flight *
        2 * math.pi * _rf_frequency)
    adj_elect02 = -adj_elect01
end

-- SIMION other actions segment.
function segment.other_actions()
    if _pressure_pa == 0 then    -- no gas
        return
    end

    -- Compute ion velocity
    local speed_ion = sqrt(ion_vx_mm^2 + ion_vy_mm^2 + ion_vz_mm^2)
    if speed_ion < 1E-7 then
        speed_ion = 1E-7    -- prevent dividing by zero
    end

    -- Compute ion kinetic energy
    local kenergy_ion_eV = (speed_ion^2) * 0.0051722 * ion_mass

    -- Compute ion distance from center
    local distance_ion_mm = sqrt(ion_px_mm^2 + ion_py_mm^2)

    -- Compute mean-free-path and effective velocity (mm/us).
    -- Only recompute if speed_ion has changed significantly.
    if last_ion_number ~= ion_number or
        abs(speed_ion / last_speed_ion - 1) > 0.05    -- significant change
    then
        mean_free_path_mm = (1000 * k * _temperature_k /
            (_pressure_pa * _sigma_m2))
        v_eff = sqrt(speed_ion^2 + 8*k*_temperature_k /
            (math.pi*_gas_mass_amu*kg_amu*1000000))
        last_speed_ion = speed_ion
        last_ion_number = ion_number
    end

    results_file:write(ion_time_of_flight.." "..mean_free_path_mm.." "
        ..speed_ion.." "..kenergy_ion_eV.." "..distance_ion_mm.." "
        ..ion_py_mm.." "..ion_pz_mm.."\\n")
    results_file:flush()

```

```

-- Limit time-step size to a fraction of the MFP.
max_timestep = mean_free_path_mm / v_eff / _steps_per_MFP

-- Probability of collision in current time-step.
local collision_prob = 1 - exp(- v_eff * ion_time_step /
                               mean_free_path_mm)

-- Test for collision.
if rand() > collision_prob then
    return -- no collision
end

-- Compute standard deviation of buffer gas velocity sqrt(kT/m).
local vr_stdev_gas =
    sqrt(k * _temperature_k / (_gas_mass_amu * kg_amu)) / 1000
local vx_gas, vy_gas, vz_gas
local scale = speed_ion + vr_stdev_gas * 1.732 * 3 --sqrt(3)=~1.732
repeat
    vx_gas = gaussian_random() * vr_stdev_gas
    vy_gas = gaussian_random() * vr_stdev_gas
    vz_gas = gaussian_random() * vr_stdev_gas
    local len = sqrt((vx_gas - ion_vx_mm)^2 + (vy_gas - ion_vy_mm)^2
                    + (vz_gas - ion_vz_mm)^2)
until rand() < len / scale

-- 0 is a head-on collision; 1 would be a near miss.
local impact_offset = sqrt(0.999999999 * rand())

-- 0 is a head-on collision; +pi/2 would be a near miss.
local impact_angle = asin(impact_offset)

-- Compute randomized angle [0, 2*pi] around radial axis.
local impact_theta = 2*math.pi*rand()

-- Convert from lab frame (L) to frame where gas particle at rest (R).
local vx = ion_vx_mm - vx_gas
local vy = ion_vy_mm - vy_gas
local vz = ion_vz_mm - vz_gas

-- Convert to polar coordinates.
local speed_ion_r, az_ion_r, el_ion_r = rect3d_to_polar3d(vx, vy, vz)

local vr_ion = speed_ion_r * cos(impact_angle) -- radial velocity
local vt_ion = speed_ion_r * sin(impact_angle) -- normal velocity
local vr_ion2 = (vr_ion * (ion_mass - _gas_mass_amu))
                / (ion_mass + _gas_mass_amu) -- new radial velocity

```

```

-- Go to reference frame in plane of vr, vt (P).
-- Rotate original ion velocity vector onto the +y axis (Y).
vx, vy, vz = elevation_rotate(90 - deg(impact_angle), vr_ion2, vt_ion, 0)

-- Deflection
vx, vy, vz = azimuth_rotate(deg(impact_theta), vx, vy, vz)

-- Transform frame back (Y) -> (P) -> (R).
vx, vy, vz = elevation_rotate(-90 + el_ion_r, vx, vy, vz)
vx, vy, vz = azimuth_rotate(az_ion_r, vx, vy, vz)

-- Go back to original frame (R) -> (L) and set velocity.
ion_vx_mm = vx + vx_gas
ion_vy_mm = vy + vy_gas
ion_vz_mm = vz + vz_gas

if _mark_collisions ~= 0 then
    mark() -- mark collisions
end
end

-- SIMION terminate segment.
function segment.terminate()
    results_file:close()
end
end

```

The background gas mean velocity is assumed to be zero. Additional information and derivations of the formulas used can be found in [42] and [36]. The approximation for the effective velocity  $v_{\text{eff}}$  is justified in [33].



# Bibliography

- [1] W. Kutschera, “Applications of Accelerator Mass Spectrometry,” *International Journal of Mass Spectrometry*, vol. 349-350, pp. 203–218, 2013.
- [2] O. Forstner, H. Gnaser, R. Golser, D. Hanstorp, M. Martschini, A. Priller, J. Rohlén, P. Steier, C. Vockenhuber, and A. Wallner, “Reassessment of  $^{182}\text{Hf}$  AMS measurements at VERA,” *Nuclear Instruments and Methods in Physics Research Section B: Beam Interactions with Materials and Atoms*, vol. 269, no. 24, pp. 3180 – 3182, 2011.
- [3] A. Galindo-Uribarri, J. Beene, M. Danchev, J. Doupé, B. Fuentes, J. G. del Campo, P. Hausladen, R. Juras, J. Liang, A. Litherland, Y. Liu, M. Meigs, G. Mills, P. Mueller, E. Padilla-Rodal, J. Pavan, J. Sinclair, and D. Stracener, “Pushing the limits of accelerator mass spectrometry,” *Nuclear Instruments and Methods in Physics Research Section B: Beam Interactions with Materials and Atoms*, vol. 259, no. 1, pp. 123 – 130, 2007.
- [4] E. Schmidt, *AMS detection of  $^{10}\text{Be}$  with a SiN-foil stack*. University of Vienna: Master Thesis, 2013.
- [5] J. Buchriegler, *Construction of a Multi-Anode Ionization Chamber for AMS at VERA*. University of Vienna: Master Thesis, 2013.
- [6] A. Litherland, I. Tomsaki, X.-L. Zhao, L. M. Cousins, J. Doupé, G. Javahery, and W. Kieser, “Isobar separation at very low energy for AMS,” *Nuclear Instruments and Methods in Physics Research Section B: Beam Interactions with Materials and Atoms*, vol. 259, no. 1, pp. 230 – 235, 2007.
- [7] J. Eliades, A. Litherland, W. Kieser, L. Cousins, S. Ye, and X.-L. Zhao, “Cl/S isobar separation using an on-line reaction cell for  $^{36}\text{Cl}$  measurement at low energies,” *Nuclear Instruments and Methods in Physics Research Section B: Beam Interactions with Materials and Atoms*, vol. 268, no. 7–8, pp. 839 – 842, 2010.
- [8] W. Kieser, X. Zhao, A. Litherland, J. Eliades, and R. Cornett, “RFQ Reaction Cells for AMS: Developments and Applications,” *EPJ Web of Conferences*, vol. 63, p. 03005, 2013.
- [9] D. Berkovits, E. Boaretto, G. Hollos, W. Kutschera, R. Naaman, M. Paul, and Z. Vager, “Selective suppression of negative ions by lasers,” *Nuclear Instruments and Methods in Physics Research Section A: Accelerators, Spectrometers, Detectors and Associated Equipment*, vol. 281, no. 3, pp. 663 – 666, 1989.
- [10] D. Berkovits, E. Boaretto, G. Hollos, W. Kutschera, R. Naaman, M. Paul, and Z. Vager, “Study of laser interaction with negative ions,” *Nuclear Instruments and Methods in Physics Research Section B: Beam Interactions with Materials and Atoms*, vol. 52, no. 3–4, pp. 378 – 383, 1990.

## BIBLIOGRAPHY

---

- [11] Y. Liu, J. R. Beene, C. C. Havener, and J. F. Liang, “Isobar suppression by photodetachment in a gas-filled rf quadrupole ion guide,” *Applied Physics Letters*, vol. 87, no. 11, 2005.
- [12] J. Rienstra-Kiracofe, G. S. Tschumper, and H. Schaefer, “Atomic and Molecular Electron Affinities: Photoelectron Experiments and Theoretical Computations,” *Chemical Reviews*, vol. 102, pp. 231 – 282, 2002.
- [13] T. Andersen, H. Haugen, and H. Hotop, “Binding Energies in Atomic Negative Ions: III,” *Journal of Physical and Chemical Reference Data*, vol. 28, no. 6, pp. 1511 – 1533, 1999.
- [14] J. Lahner, *A neutral particle detector for photodetachment studies*. University of Vienna: Master Thesis, 2014.
- [15] R. Middleton, *A Negative-Ion Cookbook*. Philadelphia, PA 19104: Department Of Physics, University of Pennsylvania, 1989.
- [16] K. Knie, T. Faestermann, and G. Korschinek, “AMS at the Munich gas-filled analyzing magnet system GAMS,”
- [17] A. Wallner, M. Bichler, K. Buczak, R. Dressler, K. Fifield, L. D. Schumann, H. Sterba, J. G. Tims, S. G. Wallner, and W. Kutschera, “Settling the Half-Life of  $^{60}\text{Fe}$ : Fundamental for a Versatile Astrophysical Chronometer,” *Physical Review Letters*, vol. 114, p. 041101, 2015.
- [18] P. Gartenmann, C. Schnabel, M. Suter, and H.-A. Synal, “ $^{60}\text{Fe}$  measurements with an EN tandem accelerator,” *Nuclear Instruments and Methods in Physics Research Section B: Beam Interactions with Materials and Atoms*, vol. 123, no. 1–4, pp. 132 – 136, 1997.
- [19] C. Vockenhuber, F. Oberli, M. Bichler, I. Ahmad, G. Quitté, M. Meier, A. N. Halliday, D.-C. Lee, W. Kutschera, P. Steier, R. J. Gehrke, and R. G. Helmer, “New Half-Life Measurement of  $^{182}\text{Hf}$ : Improved Chronometer for the Early Solar System,” *Physical Review Letters*, vol. 93, p. 172501, Oct 2004.
- [20] C. Vockenhuber, M. Bichler, R. Golser, W. Kutschera, A. Priller, P. Steier, and S. Winkler, “ $^{182}\text{Hf}$ , a new isotope for AMS,” *Nuclear Instruments and Methods in Physics Research Section B: Beam Interactions with Materials and Atoms*, vol. 223–224, no. 0, pp. 823 – 828, 2004. Proceedings of the Ninth International Conference on Accelerator Mass Spectrometry.
- [21] H. Chen, P. Andersson, A. O. Lindahl, and D. Hanstorp, “The electronic structure of  $\text{HfF}_5^-$  and  $\text{WF}_5^-$ ,” *Chemical Physics Letters*, vol. 511, no. 4–6, pp. 196 – 200, 2011.
- [22] T. Leopold, J. Rohlén, P. Andersson, C. Diehl, M. Eklund, O. Forstner, D. Hanstorp, H. Hultgren, P. Klason, A. Lindahl, and K. Wendt, “Feasibility of photodetachment isobar suppression of  $\text{WF}$  with respect to  $\text{HfF}$ ,” *International Journal of Mass Spectrometry*, vol. 359, no. 0, pp. 12 – 18, 2014.
- [23] M. Gutovski, P. Skurski, X. Li, and L. Wang, “ $(\text{MgO})_n^-$  ( $n=1-5$ ) Clusters: Multipole-Bound Anions and Photodetachment Spectroscopy,” *Physical Review Letters*, vol. 85, no. 15, pp. 3145 – 3148, 2000.

- [24] F. Major, V. Gheorghe, and G. Werth, *Charged Particle Traps*. Heidelberg: Springer, 2006.
- [25] F. M. Arscott, *Periodic Differential Equations, An introduction to Mathieu, Lamé and Allied Functions*. Oxford: Pergamon Press, 1964.
- [26] N. W. McLachlan, *Theory and Application of Mathieu Functions*. New York: Dover Publications, 1964.
- [27] D. R. Denison, “Operating Parameters of a Quadrupole in a Grounded Cylindrical Housing,” *Journal of Vacuum Science and Technology*, vol. 8, no. 1, pp. 266–269, 1971.
- [28] F. Herfurth, J. Dilling, A. Kellerbauer, G. Bollen, S. Henry, H.-J. Kluge, E. Lamour, D. Lunney, R. Moore, C. Scheidenberger, S. Schwarz, G. Sikler, and J. Szerypo, “A linear radiofrequency ion trap for accumulation, bunching, and emittance improvement of radioactive ion beams,” *Nuclear Instruments and Methods in Physics Research Section A: Accelerators, Spectrometers, Detectors and Associated Equipment*, vol. 469, no. 2, pp. 254 – 275, 2001.
- [29] Y. Liu, J. Liang, G. Alton, J. Beene, Z. Zhou, and H. Wollnik, “Collisional cooling of negative-ion beams,” *Nuclear Instruments and Methods in Physics Research Section B: Beam Interactions with Materials and Atoms*, vol. 187, no. 1, pp. 117 – 131, 2002.
- [30] A. Nieminen, J. Huikari, A. Jokinen, J. Äystö, P. Campbell, and E. Cochrane, “Beam cooler for low-energy radioactive ions,” *Nuclear Instruments and Methods in Physics Research Section A: Accelerators, Spectrometers, Detectors and Associated Equipment*, vol. 469, no. 2, pp. 244 – 253, 2001.
- [31] R. Iffländer and G. Werth, “Optical Detection of Ions Confined in a RF Quadrupole Trap,” *Metrologia*, vol. 13, pp. 167–170, 1977.
- [32] A. Kellerbauer, T. Kim, R. Moore, and P. Varfalvy, “Buffer gas cooling of ion beams,” *Nuclear Instruments and Methods in Physics Research Section A: Accelerators, Spectrometers, Detectors and Associated Equipment*, vol. 469, no. 2, pp. 276 – 285, 2001.
- [33] S. Schwarz, *Simulations for Ion Traps - Buffer Gas Cooling*, vol. 749 of *Lecture Notes in Physics*. Berlin Heidelberg: Springer-Verlag, 2008.
- [34] H. Ellis, R. Pai, E. McDaniel, E. Mason, and L. Viehland, “Transport properties of gaseous ions over a wide energy range,” *Atomic Data and Nuclear Data Tables*, vol. 17, no. 3, pp. 177 – 210, 1976.
- [35] J. F. Ziegler, M. Ziegler, and J. Biersack, “SRIM – The stopping and range of ions in matter (2010) ,” *Nuclear Instruments and Methods in Physics Research Section B: Beam Interactions with Materials and Atoms*, vol. 268, no. 11–12, pp. 1818 – 1823, 2010.
- [36] D. Manura, *Additional Notes on the SIMION Collision Model HS1*. Scientific Instrument Services, Inc., 2007.
- [37] A. Bondi, “van der Waals Volumes and Radii,” *The Journal of Physical Chemistry*, vol. 68, no. 3, pp. 441–451, 1964.

## BIBLIOGRAPHY

---

- [38] R. D. Shannon, “Revised effective ionic radii and systematic studies of interatomic distances in halides and chalcogenides,” *Acta Crystallographica Section A*, vol. 32, no. 5, pp. 751–767, 1976.
- [39] D. Manura and D. Dahl, *SIMION<sup>®</sup> Version 8.0/8.1*. Ringoes, NJ 08551: Scientific Instrument Services, 2011.
- [40] D. Lunney, C. Bachelet, C. Guénaut, S. Henry, and M. Sewtz, “COLETTE: A linear Paul-trap beam cooler for the on-line mass spectrometer MISTRAL,” *Nuclear Instruments and Methods in Physics Research Section A: Accelerators, Spectrometers, Detectors and Associated Equipment*, vol. 598, pp. 379–387, 2009.
- [41] M. L. Seman and L. M. Branscomb, “Structure and photodetachment spectrum of the atomic carbon negative ion,” *Physical Review*, vol. 125, pp. 1602–1608, 1962.
- [42] “SIMION 8.1 Supplemental Documentation on Collision Model HS1.” [http://simion.com/info/collision\\_model\\_hs1.html](http://simion.com/info/collision_model_hs1.html). Accessed: 2015-01-03.

# Curriculum Vitae

## Education

### University of Vienna

M.Sc., Physics, April 2013 - present

*Thesis Topic:* Laser Photodetachment in a Gas-Filled RF-Quadrupole

*Supervisor:* Univ.-Prof. Dipl.-Ing. Dr. Robin Golser

B.Sc., Physics, October 2009 - April 2013

*Thesis Topic:* Charge State Distribution of Carbon after an Argon Stripper

*Supervisor:* Ass.-Prof. Mag. Dr. Peter Steier

### Bundesrealgymnasium Traun

Graduation (Matura) *with distinction*, June 2009

## Internships

### GSI Helmholtzzentrum für Schwerionenforschung

HGS-HIRe Summer Student Program, August 5 - September 26, 2013

*Project:* Setup of a Low-Energy Ion Beamline for Heavy, Highly Charged Ions

*Supervisor:* Dr. Zoran Andelkovic

### VERA Laboratory, University of Vienna

Summer Internship, August 1 - 29, 2012

*Project:* Investigations on Charge State Distributions of Uranium and Thorium for AMS Measurements

*Supervisor:* Ass.-Prof. Mag. Dr. Peter Steier

## Scholarships

Performance Scholarships, University of Vienna, awarded in 2012, 2013 and 2015

## Teaching Experience

### University of Vienna

Frauentutorium Physik Bachelor und Lehramt, WS 2013 and WS 2014

Einführung in die Physik 3 - Tutorium, WS 2013 and WS 2014

## Conferences and Talks

**Annual Meeting of the Austrian Physical Society**, September 24 - 27, 2014,  
Pöllau, Austria

*Talk:* Laser Photodetachment in a Gas-Filled RF-Quadrupole for AMS

**Seminar Talk**, October 30, 2014, VERA Laboratory, Vienna, Austria

*Talk:* The ILIAS project: selective laser photodetachment in an RFQ ion cooler

**Seminar Talk**, February 26, 2015, CERN-ISOLDE, Geneva, Switzerland

*Talk:* Selective laser photodetachment in an RFQ ion beam cooler for AMS

**Spring Meeting of the German Physical Society**, March 23 - 27, 2015,  
Heidelberg, Germany

*Talk:* An ion beam cooler for negatively charged atomic and molecular ions

## Papers

**The ILIAS project for selective isobar suppression by laser photodetachment**,  
O. Forstner, P. Andersson, D. Hanstorp, J. Lahner, M. Martschini, J. Pitters, A. Priller,  
P. Steier, R. Golser, Nucl. Instr. and Meth. B (2015), *in press*

**He stripping for AMS of  $^{236}\text{U}$  and other actinides using a 3 MV tandem accelerator**,  
S. Winkler, P. Steier, J. Buchriegler, J. Lachner, J. Pitters, A. Priller, R. Golser,  
Nucl. Instr. and Meth. B (2015), *accepted*